

Galaxy size and rotation curve diversity in Λ CDM with baryons

AKAXIA CRUZ ^{1,2,3} ALYSON M. BROOKS ^{1,4} MARIANGELA LISANTI ^{1,2} ANNIKA H. G. PETER ^{5,6,7}
ROBEL GEDA ³ THOMAS QUINN ⁸ MICHAEL TREMMEL ⁹ FERAH MUNSHI ¹⁰ BEN KELLER ¹¹ AND
JAMES WADSLEY ¹²

¹Center for Computational Astrophysics, Flatiron Institute, New York, NY 10010, USA

²Department of Physics, Princeton University, Princeton, NJ 08544, USA

³Department of Astrophysical Sciences, Princeton University, Princeton, NJ 08544, USA

⁴Department of Physics & Astronomy, Rutgers, the State University of New Jersey, Piscataway, NJ 08854, USA

⁵Department of Physics, Ohio State University, Columbus, OH 43210, USA

⁶Department of Astronomy, Ohio State University, Columbus, OH 43210, USA

⁷Center for Cosmology and AstroParticle Physics (CCAPP), The Ohio State University, Columbus, OH 43210, USA

⁸Department of Astronomy, University of Washington, Seattle, WA 98195, USA

⁹School of Physics, University College Cork, Ireland

¹⁰Department of Physics & Astronomy, George Mason University, Fairfax, VA 22030, USA

¹¹Department of Physics and Material Science, The University of Memphis, Memphis, TN 38152, USA

¹²Department of Physics and Astronomy, McMaster University, Ontario, Canada

ABSTRACT

Observed rotation curves of dwarf galaxies exhibit significant diversity at fixed halo mass, challenging galaxy formation within the Cold Dark Matter (CDM) model. Previous cosmological galaxy formation simulations with baryonic physics fail to reproduce the full diversity of rotation curves, suggesting either that there is a flaw in baryonic feedback models, or that an alternative to CDM must be invoked. In this work, we use the Marvelous Massive Dwarf zoom-in simulations, a suite of high-resolution dwarf simulations with $M_{200} \sim 10^{10}\text{--}10^{11} M_{\odot}$ and $M_{*} \sim 10^7\text{--}10^9 M_{\odot}$, designed to target the mass range where galaxy rotation curve diversity is maximized, i.e., between $V_{\max} \sim 70\text{--}100$ km/s. We add to this a set of low-mass galaxies from the Marvel Dwarf Zoom Volumes to extend the galaxy mass range to lower values. Our fiducial star formation and feedback models produce simulated dwarfs with a broader range of rotation curve shapes, similar to observations. These are the first simulations that can both create dark matter cores via baryonic feedback, reproducing the slower rising rotation curves, while also allowing for compact galaxies and steeply rising rotation curves. Our simulated dwarfs also reproduce the observed size- M_{*} relation, including scatter, producing both extended and compact dwarfs for the first time in simulated field dwarfs. We explore star formation and feedback models and conclude that previous simulations may have had feedback that was too strong to produce compact dwarfs.

1. INTRODUCTION

Observations showing that rotation curves (RCs) are flat at large radii provided some of the first evidence for more matter in galaxies than can be accounted for by gas and stars (Rubin et al. 1980; Bosma 1981). Since then, it has been determined that dark matter comprises $\sim 85\%$ of all matter in the Universe (Planck Collaboration et al. 2020). The Cold Dark Matter (CDM) model describes the Universe well on large scales (e.g., Springel et al. 2006), but has encountered trouble explaining the diversity of RC shapes, particularly in dwarf galaxies (Sales et al. 2022). Dark matter-only (DMO) simulations show universal, self-similar halo density profiles (NFW pro-

files, Navarro et al. 1996, 1997) that are steeper than some inferred from the RCs of dwarf galaxies (Moore 1994; Flores & Primack 1994; de Blok et al. 2001; de Blok 2010; Oh et al. 2011). Hydrodynamic simulations have shown that the inclusion of energetic feedback from baryons can fluctuate the gravitational potential at the centers of dwarf galaxies, transforming an initially steep density profile into a more shallow profile, thought to reconcile simulations with slowly rising RCs (Read & Gilmore 2005; Mashchenko et al. 2008; Governato et al. 2012; Pontzen & Governato 2012; Teyssier et al. 2013; Di Cintio et al. 2014a; Tollet et al. 2016; Read et al. 2016a; Benítez-Llambay et al. 2019; Dutton et al. 2019).

However, it has more recently been recognized that the full range of RCs, from quickly to slowly rising, has not been fully reproduced by galaxy simulations (Oman et al. 2015; Santos-Santos et al. 2018, 2020). In particular, Oman et al. (2015) highlights the diversity of observed RCs, showing that diversity is maximized at V_{\max} (the maximum observed RC velocity) $\sim 70\text{--}80$ km/s, with a factor ~ 4 spread within the central 2 kpc ($V_{2\text{kpc}}$) at this fixed V_{\max} . A similar central velocity spread relative to V_{\max} is found in Spitzer Photometry and Accurate RCs (SPARC, Lelli et al. 2016a), as well as more recent H α RCs (Relatores et al. 2019a,b).

Previous simulations with CDM and baryons have struggled to reproduce the full range of observed diversity of RCs. In particular, Oman et al. (2015) found a lack of diversity in the Evolution and Assembly of GaLaxies and their Environments (EAGLE, Schaye et al. 2015; Crain et al. 2015) simulations, though they explicitly used simulations that do not transform dark matter cusps into cores. Santos-Santos et al. (2018) examined diversity in the Numerical Investigation of a Hundred Astrophysical Objects (NIHAO, Wang et al. 2015) simulations, which do create dark matter cores (e.g., Di Cintio et al. 2014a,b). They demonstrated that using the gravitational midplane potential to calculate RCs better modeled dwarf galaxies that were out of dynamical equilibrium due to bursty feedback, as opposed to using shells of enclosed mass that assume spherical symmetry. No matter the RC calculation method, the NIHAO simulations fail to capture the RCs that rise more quickly than predicted by NFW (see also Frosst et al. 2022). Likewise, Santos-Santos et al. (2020) showed that EAGLE simulations with a high density threshold for star formation (the gas density above which stars form) can produce cored dark matter profiles with slowly rising RCs, but struggle to simultaneously produce the most quickly rising RCs. In contrast, simulations with lower density thresholds for star formation are able to produce the more quickly rising RCs but not the more slowly rising ones. Similarly, Roper et al. (2023) showed a correspondence between high (low) star formation density threshold and slowly (quickly) rising RCs. Further, Roper et al. (2023) showed that simulations that do not create dark matter cores can reproduce the full range of observed diversity due to non-circular motions introduced in mock HI observations.

SPARC suggests an additional observed diversity in the galaxy size–stellar mass plane. Observations show the presence of both compact and extended galaxies at a given stellar mass (M_*). Previous hydrodynamical simulations within CDM struggle not only to produce diversity in RCs, but also diversity in the size–

M_* plane (Sales et al. 2022). Jiang et al. (2019) showed that NIHAO, and Feedback in Realistic Environments 2 (FIRE-2, Hopkins et al. 2018) and simulations presented in Lupi et al. (2017) produce galaxies that are more diffuse than observed galaxies and struggle to produce the most compact galaxies at and below $M_* \sim 10^9 M_\odot$.

In this work, we use high-resolution hydrodynamical, cosmological simulations of dwarf galaxies produced using the CHANGA code with multiple feedback models to examine the diversity of RCs and galaxy sizes compared to observations. We show that a new suite of dwarf galaxies, the Marvelous Massive Dwarf zooms, produce a range of both quickly and slowly rising RCs at a given halo mass when run with our fiducial model. This suite is the first to reproduce a broad range of RC diversity in CDM with baryons, and without creating mock HI observations. In addition, the galaxies also produce a more realistic range of sizes at stellar masses $M_* \sim 10^7\text{--}10^9 M_\odot$, consistent with the scatter showing both extended and compact galaxies in observations.

This paper is organized as follows. In Section 2, we detail the galaxy formation models used in our simulated sample. In Section 3, we briefly describe the observational data with which we compare our simulated results. We detail our analysis techniques used throughout this work in Section 4. We present our RC diversity shapes in Section 5.1 and explore the impact of baryons on RC shapes in Section 5.2. In Section 5.3, we then discuss diversity in the size– M_* plane, and in Section 6, we consider how subgrid physics can prevent the formation of compact galaxies. We discuss how our results compare to previous works in CDM with baryons and in alternative dark matter models in Section 7, and finally summarize our results in Section 8. In Appendix A, we detail how the method used to obtain RCs influences their shapes. In Appendix B, we briefly discuss feedback differences on RC shape. In Appendix C, we detail our density profiles and fitting procedure and show RC shape trends with dark matter density slope.

2. SIMULATIONS

In this study, we use two suites of simulated dwarf galaxies: one collection of “zoom volumes” and a complementary set of more massive individual zoom-in galaxy simulations. Both suites are produced using the N-body+Smooth Particle Hydrodynamics (SPH) code Charm Nbody Gravity solver (CHANGA, Menon et al. 2015) which adopts hydrodynamic physics from GASOLINE2 (Wadsley et al. 2004, 2017), but modified to use the CHARM++ runtime code for load balancing and communication. All simulations are run in a fully cosmologi-

cal context. We run with a fiducial model on which most of the results are based, but also rerun two galaxies with varying subgrid physics in Section 6. First, we detail the physics in common between the two simulation suites, then discuss their differences in Sections 2.1 and 2.2. In Section 2.3, we describe the additional variations used for the tests in Section 6. The final sample selection compared to the SPARC data (Lelli et al. 2016a, see Section 3) is defined in Section 4.

The fiducial star formation model for both simulation suites utilizes the metal-line-cooling and star formation scheme as presented in Christensen et al. (2012). This model includes non-equilibrium formation and destruction of H_2 and a uniform time-dependent UV field (Haardt & Madau 2012) to model photoionization and heating. Lyman-Werner radiation from young stars is additionally tracked and can further heat and photo-dissociate H_2 and suppress star formation, mimicking early stellar feedback. Star particles represent stellar populations with a Kroupa (2001) initial mass function. The star particle initial mass is 30% of the original gas particle mass. Mass and metals from stars are returned to surrounding gas particles in winds and in Type I and Type II supernovae (SNe) (Stinson et al. 2006).

Star formation is restricted to occur stochastically in the presence of H_2 when gas particles become cold ($T_* \leq 10^3$ K) and dense ($n_* \geq 0.1 \text{ cm}^{-3}$). The probability of creating a star particle (with mass m_{star}) from a gas particle (with mass m_{gas}) with local dynamical time, t_{dyn} , in time $\Delta t = 10^6$ yr is:

$$p = \frac{m_{\text{gas}}}{m_{\text{star}}} (1 - e^{-c_* X_{H_2} \Delta t / t_{\text{dyn}}}), \quad (1)$$

where the value adopted for star formation efficiency is $c_* = 0.1$. The star formation efficiency, c_* , times the fraction of non-ionized molecular hydrogen, X_{H_2} , produces the appropriate normalization of the Kennicutt-Schmidt relation (Christensen et al. 2014). Although the density threshold is low compared to other bursty star formation prescriptions (e.g., Governato et al. 2010; Benítez-Llambay et al. 2019; Dutton et al. 2019, 2020), the actual density of star-forming gas tends to be closer to 100 cm^{-3} due to the additional requirement that H_2 be present.

All of the simulations in our zoom volume and fiducial zoom-in models include black hole (BH) formation and growth, with BH accretion and feedback models from Tremmel et al. (2015) and Tremmel et al. (2017). We do not make assumptions about BH halo occupation fractions. Instead, BH seed formation is related to the physical state of the gas (i.e., temperature, density, metallicity, molecular fraction) at high redshift.

The BHs are subject to a prescription of dynamical friction which follows the orbital evolution of BHs, as introduced by Tremmel et al. (2015). Correctly accounting for this effect can lead to pairs of supermassive BHs at kpc-scale separations that survive for several Gyrs (Tremmel et al. 2018). BHs in our simulation also obey a modified Bondi accretion (Tremmel et al. 2017). Parameters for seeding and accretion are detailed for each simulation suite below.

Here, we have described the physics that the simulations have in common. Below, we describe the differences between the two suites. In summary, they use slightly different cosmologies and resolutions, they have slightly different seeding mechanisms for BHs, and their feedback implementation (for Type II SNe and BHs) is different. Despite that, previous works have used both sets of simulations simultaneously to increase the mass range of the simulated sample size. They were unable to find differences in galaxy properties between the two runs, e.g., in stellar-to-halo mass, HI content and gas fractions, sizes, or metallicity (see Piacitelli et al. 2025; Ruan et al. 2025). We again combine them in this work to increase the range of galaxy masses and explore potential differences (see Appendix B.)

2.1. *Marvel Dwarf Zoom Volumes*

The Marvel dwarf suite (hereafter Marvel) consists of a population of dwarfs from “zoom volumes” (Bellovary et al. 2019; Munshi et al. 2021; Christensen et al. 2024). In contrast to typical zoom simulations that focus their Lagrangian regions on individual halos, in these simulations, the Lagrangian regions are larger volumes that contain dozens of dwarf galaxies. The volumes for the Marvel zooms are selected to be between ~ 1.5 –7 Mpc away from Milky Way-mass galaxies (Christensen et al. 2024). These volumes represent isolated local-volume galaxies. Four such simulations are run, named CptMarvel, Elektra, Rogue, and Storm, with a WMAP3 cosmology ($\Omega_\Lambda = 0.736$, $\Omega_m = 0.264$, $\Omega_b = 0.0441$, $\sigma_8 = 0.805$, $n_s = 0.967$, $h = 0.712$, Spergel et al. 2007). Each zoom volume has a spline force softening of $\epsilon = 60$ pc, an initial gas mass resolution of $1410 M_\odot$, an initial stellar mass resolution of $420 M_\odot$, and a dark matter mass resolution of $6650 M_\odot$.

The Marvel simulations include a model for stellar feedback from Type II SNe, which adopts a “blastwave” implementation as detailed in Stinson et al. (2006). This model deposits mass, thermal energy, and metals into nearby gas when a massive star of 8–40 M_\odot becomes a SN. Each SN releases 1.5×10^{51} ergs of energy into 32 neighboring gas particles, and a star particle deposits 1.5×10^{49} ergs/ M_\odot over the lifetime of SNe II. After

each SN, gas cooling is turned off for a time determined by Equation 11 in [Stinson et al. \(2006\)](#), the timescale over which the gas particle does not radiatively cool. The deposited energy, combined with the turning off of cooling, is used to mimic how inefficient cooling influences the local interstellar medium (ISM). The Storm zoom volume is additionally run with superbubble feedback, which is introduced in the next subsection.

BH seeds form in the early universe if the gas particle has already met the star formation threshold. Additionally, BH particles form in extremely dense ($n > 1.5 \times 10^4 \text{ cm}^{-3}$) and cool ($T < 2 \times 10^4 \text{ K}$) gas regions. To prevent fragmentation into stars, gas particles that can form BHs must also have low metallicity ($Z < 10^{-4}$) and have low molecular fraction ($X_{H_2} < 10^{-4}$). The mass of a BH seed is $5 \times 10^4 M_\odot$. BHs accrete according to a modified Bondi-Hoyle accretion, which accounts for the rotational support of the surrounding gas ([Tremmel et al. 2017](#)). The energy of accretion onto the BHs is isotropically transferred to nearby gas particles as thermal energy using the blastwave feedback model of [Stinson et al. \(2006\)](#) for the Marvel zoom volumes. However, [Bellovary et al. \(2019\)](#) found that BHs in Marvel zoom volumes barely grow after their formation and thus impart very little energy.

2.2. The Marvelous Massive and Extended Dwarf Zooms

We analyze the Marvelous Massive Dwarf zooms, a collection of 40 zoom-in simulations with $M_{200} \sim (0.1\text{--}2) \times 10^{11} M_\odot$ and stellar masses $M_* \sim (0.06\text{--}3) \times 10^9 M_\odot$, as well as the Extended Marvelous Dwarf zooms that have stellar masses down to $M_* \sim 6 \times 10^6 M_\odot$. As suggested by the name, the Marvelous Massive Dwarfs are designed to have higher masses than the Marvel set. They are specifically run to investigate the mass range where the diversity of RCs is maximized and selected based on their stellar mass, aiming for $10^8\text{--}10^9 M_\odot$. Both the Marvelous Massive and Extended Marvelous dwarf zooms are selected from the $(25 \text{ Mpc})^3$ box, Romulus25 ([Tremmel et al. 2017](#)). We choose halos that are at least 1.5 Mpc away from any galaxy with $M_* > 10^{10} M_\odot$ at redshift $z = 0.1$. At a fixed stellar mass, they are chosen to span a range in halo mass. No other selection criteria are used. Since they are run with the same physics, we refer to the Marvelous Massive Dwarf zooms and the Extended Marvelous Dwarf zooms collectively as the Marvelous Massive Dwarf zooms or just the Massive Dwarfs to not confuse results with previous work using the Marvel zoom-volume galaxies.

These 55 simulations are run at “Mint” resolution with spline force softening of $\epsilon = 87 \text{ pc}$, an initial gas

mass resolution of $3300 M_\odot$, an initial stellar mass resolution of $990 M_\odot$, and a dark matter mass resolution of $1.8 \times 10^4 M_\odot$. All of our Marvelous Massive Dwarf zooms are run with a Planck Cosmology ($\Omega_\Lambda = 0.6914$, $\Omega_m = 0.3086$, $\Omega_b = 0.04825$, $\sigma_8 = 0.8288$, $n_s = 0.9611$, $h = 0.6777$, [Planck Collaboration et al. 2014](#)) and used the “zoom-in” methods described by [Pontzen et al. \(2008\)](#).

We run the 40 Marvelous Massive Dwarf zooms and the 15 Extended Marvelous Dwarf zooms with a fiducial model that includes H_2 cooling, star formation, and superbubble feedback. Stars preferentially form in clusters ([Pfalzner et al. 2012](#); [Krause et al. 2020](#)). Feedback from clustered stars produces superbubbles, which are distinct from isolated SNe, as modeled by the blastwave model. The superbubble feedback model used here ([Keller et al. 2014](#)) introduces a multiphase treatment of gas, evaporation, and thermal conduction. Unlike the blastwave model, this feedback model does not explicitly shut off cooling. Instead, the evaporation from thermal conduction is designed to regulate the amount of hot gas. As in [Keller et al. \(2014\)](#), a star particle deposits $10^{49} \text{ erg}/M_\odot$ of thermal energy due to SNeII. This model deposits feedback into resolution elements in a brief multi-phase state: the particles have different specific energies, masses, and densities in the hot bubble phase and the cold ISM phase. Then, for each phase, separate cooling rates can be derived using their respective densities and temperatures. Gas particles become single phase again when the hot phase either cools or evaporates the cool phase.

BH particles form in gas particles with high density ($n > 1.5 \times 10^4 \text{ cm}^{-3}$), cool temperature ($T < 5 \times 10^3 \text{ K}$), low metallicity ($Z < 10^{-5}$), low molecular fraction ($X_{H_2} < 2 \times 10^{-3}$), and large Jeans mass ($M_J > 10^5 M_\odot$). These criteria are motivated by [Wise et al. \(2019\)](#); [Regan et al. \(2020\)](#); [Regan \(2023\)](#). The mass of a BH seed is $10^5 M_\odot$. BHs have a density-boosted Bondi accretion motivated by [Booth & Schaye \(2009\)](#) where the boost density threshold is 100 cm^{-3} . The energy of accretion onto the BHs is isotropically transferred to nearby gas particles as thermal energy using the superbubble feedback model of [Keller et al. \(2014\)](#) for the Massive Dwarf zooms. [Bellovary et al. \(2019\)](#) found little accretion in the Marvel galaxies, and we explored a subset of the Massive Dwarf zoom galaxies run with and without BHs and found no preferential shift in their stellar sizes or masses.

We visually examine the morphology of 40 of the most massive galaxies in the Massive Dwarf zooms, shown as mock-UVI images in [Figure 1](#). The images are “face-on” in the x-y plane, so that the angular momentum

of each galaxy is rotated into the z-direction, which is out of the page. The zooms are ordered by stellar mass, M_* , from top to bottom and left to right in a given row. The zoom-in name is annotated in the upper left of each subpanel. The details of how M_{200} and angular momentum are calculated are described in Section 4.1. From visual inspection, it can be seen that the galaxies have diverse morphologies and sizes, as a given row represents roughly the same stellar mass, and there is a diversity in size.

Beyond these galaxies having diverse morphologies, the simulations also agree well with other observables. In forthcoming work, we will demonstrate the ability to produce stellar dwarf galaxy disks (Geda et al. 2025) with stellar masses down to $10^7 M_\odot$, which are observed (Lelli et al. 2016a), but have evaded previous simulations (El-Badry et al. 2018; Benavides et al. 2025; Celiz et al. 2025). Additionally, the ChaNGa models make galaxies that are in better agreement with observed stellar age gradients in dwarfs (Riggs et al. 2024), have HI sizes and gas fractions that match observed galaxies (Ruan et al. 2025), and match the mass-metallicity relation, the sSFR-mass trends, and reasonably reproduce dwarf CGM column densities (Piacitelli et al. 2025). We have additionally made predictions for the turn down in the baryonic Tully-Fisher relationship (Ruan et al. 2025) and in stellar shapes (Keith et al. 2025), which can further test the ChaNGa models used in this work.

2.3. NIHAO Reruns

Because ChaNGa adopts hydrodynamic physics from GASOLINE, the code used for the NIHAO simulations, we can rerun initial conditions with some of the subgrid physics used in Wang et al. (2015). In Section 6, we rerun two of the Massive Dwarf zoom-in galaxies that have quiescent merger histories after cosmic time of ~ 2 Gyrs to better understand the differences between the NIHAO results and our simulations. Starting from the Mint resolution, fiducial star formation, and superbubble feedback model, we make incremental changes, progressing towards the NIHAO model and resolution. In the NIHAO star formation model, gas is eligible to form stars once it has reached specified density and temperature thresholds in agreement with the Kennicutt-Schmidt Law. In the model adopted in Wang et al. (2015), which we mimic here, stars form in cold ($T_* < 1.5 \times 10^4$ K) and dense ($n_* > 10.3 \text{ cm}^{-3}$) gas. The NIHAO star formation model deviates from our fiducial model significantly, with stars forming in much less dense and much warmer gas.

NIHAO uses the blastwave SN feedback model of Stinson et al. (2006), with star particles releasing a total of $10^{49} \text{ erg}/M_\odot$ thermal energy due to SNe II, as well as early stellar feedback from massive stars (Stinson et al. 2013). To limit star formation to agree with the abundance matching value at the Milky Way scale, the early feedback efficiency, $\epsilon_{\text{ESF}} = 13\%$, of the total stellar flux, $2 \times 10^{50} \text{ erg}/M_\odot$ is ejected into the surrounding gas over the 4 Myr between a star’s formation and when Type II SNe begin to occur. For our runs, we adopt a slightly lower $\epsilon_{\text{ESF}} = 10\%$, consistent with Stinson et al. (2013).

The NIHAO simulations are run with constant relative resolution between the gravitational softening of the dark matter ϵ_{DM} and halo virial radius across ~ 3 dex of halo mass and have $\sim 10^6$ dark matter particles per halo. This means that each halo mass scale is run at a different resolution. We approach the mass resolution of the NIHAO runs for the $M_{200} \sim 10^{10}\text{--}10^{11} M_\odot$ halos¹ by stepping from our “Mint” resolution to “Near Mint” that has half the force resolution (174 pc) and $8\times$ lower mass resolution (initial gas particle masses of $2.64 \times 10^4 M_\odot$, dark matter mass resolution of $1.4 \times 10^5 M_\odot$).

We change one subgrid physics prescription at a time to isolate the impact on stellar half-light radius and mass. Independent of resolution, in all of the runs with NIHAO subgrid physics models, we exclude BHs since the NIHAO runs we compare to do not include them (Santos-Santos et al. 2018). The details of these physics variations are discussed in Section 6.

3. OBSERVATIONAL DATA

We compare our numerical results to observed galaxies from the SPARC dataset (Lelli et al. 2016a). These observations comprise a sample of 175 nearby galaxies with homogeneous photometry at $3.6 \mu\text{m}$, which complements high-quality RC data from previous HI and/or H α observations. Since the velocity dispersion of HI is typically on the order of ~ 10 km/s, we expect pressure support to be significant only in very low-mass dwarf galaxies with rotation velocities of ~ 20 km/s (Lelli et al. 2012). However, the reported SPARC RCs have been corrected for pressure support, beam smearing, and inclination. Stellar masses are derived by assuming a mass-to-light ratio of $M_*/L_{[3.6 \mu\text{m}]} = 0.5$.

The sample of SPARC galaxies considered in this analysis only includes those with inclinations $i > 30^\circ$ as in Santos-Santos et al. (2020) and those suitable for dy-

¹ In NIHAO, $M_{200} = (2.63\text{--}7.12) \times 10^{10} M_\odot$ halos have a dark matter mass resolution of $6.426 \times 10^4 M_\odot$, baryon (gas and stars) mass resolution of $1.173 \times 10^4 M_\odot$, and a gravitational softening of $\epsilon_{\text{gas}} = 132.6$ pc for gas and $\epsilon_{\text{DM}} = 310.5$ pc for dark matter.

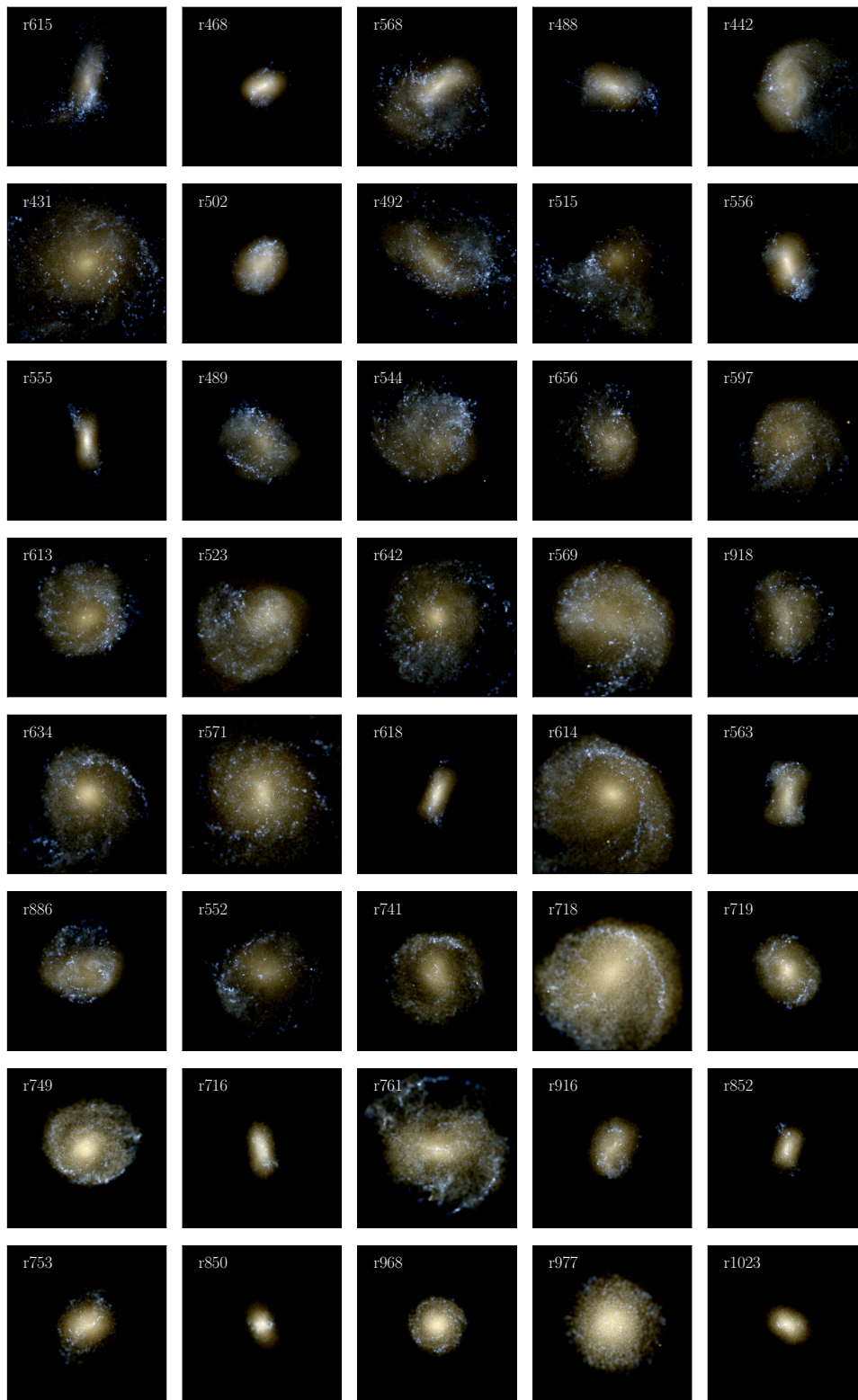


Figure 1. MOCK UVI IMAGES OF 40 OF THE MASSIVE DWARF ZOOM-IN GALAXIES AT $z = 0$, ordered by decreasing M_* from top left to bottom right. The zoom-in name is annotated in the upper left of each subpanel. Each galaxy is shown face-on (i.e., with the angular momentum vector out of the page), and each square panel has a side length of 15 kpc. Visually, it is clear that the Massive Dwarf zooms have diverse morphologies.

namical studies with quality flag $Q \neq 3$ as in Zentner et al. (2022), to minimize RCs with substantial uncertainties. We use the RCs from Lelli et al. (2016a) to calculate V_{\max} values for the observed sample. We take the maximum value of the observed RCs out to the last observed radial bin to be V_{\max} for the observed sample, noting that in some cases this value might under-predict the true maximum circular velocity. This is more common in the lower-mass galaxies, as the observational HI-limit is still on the rising part of the RC (see e.g., Ruan et al. 2025) for more details on how our simulated galaxies are impacted.

4. ANALYSIS

4.1. Halo Finding and Centering

We identify halos in a given simulation using the AMIGA halo finder (AHF; Knollmann & Knebe 2009). The virial radius, R_{vir} , of a halo is the radius at which the density corresponds to $\Delta_h = 200$ times the critical density of the Universe, ρ_c . All halos in this work are analyzed at $z = 0$. We calculate the virial mass of halos as:

$$M_{\text{vir}} = \frac{4\pi}{3} \Delta_h \rho_c R_{\text{vir}}^3. \quad (2)$$

We center each halo using the shrinking-sphere procedure (Power et al. 2003) and Lorentz boost into the rest frame of the center-of-mass of the particles within 1 kpc of the center. We then rotate the galaxy in the x–y plane such that the angular momentum vector of the gas within 5 kpc of the halo center points in the z-direction. We do produce disk galaxies and, in these systems, the z-component of the total angular momentum is well aligned with the z-direction (Geda et al. 2025). However, even for the non-disky galaxies, we use the same orientation methodology.

4.2. Rotation Curves

This subsection describes the variety of methods used to calculate the RC velocities from our simulations and how we compare them with observations. We calculate full RCs between $r \in [r_{\text{conv}}, 15 \text{ kpc}]$ using 100 linearly spaced bins. Below the convergence radius, r_{conv} , two-body scattering can alter the mass distribution (Power et al. 2003). Ludlow et al. (2019a) notes that the convergence radius interior to which we expect artificial heating can be conveniently approximated as $r_{\text{conv}} = 0.055 \times l$, where $l = L_{\text{box}}/N_{\text{part}}^{1/3}$ is the mean interparticle spacing in physical units for a simulation with box length L_{box} and N_{part} total particles. In the Massive zooms, $r_{\text{conv}} \sim 0.45 \text{ kpc}$ and in the Marvel simulations, $r_{\text{conv}} \sim 0.34 \text{ kpc}$. The upper end of the considered radial range is motivated by the radius that

corresponds to the true maximum halo velocity: we find $R_{\max} < 15 \text{ kpc}$ for all systems considered in this work. The binning scheme is chosen so that each bin contains at least 3000 dark matter particles, even for the smallest mass systems. In the higher-mass systems, each bin contains well over 3000 particles. The limit on particles-per-bin is expected to properly resolve densities (Power et al. 2003).

We calculate the RCs using two different methods and then use two separate proxies to determine the maximum and central value. First, we assume spherical symmetry and calculate

$$V^{\text{circ}}(r) = \sqrt{\frac{GM(< r)}{r}}, \quad (3)$$

where G is Newton’s constant and $M(< r)$ is the total enclosed mass at galactocentric radius r . The total enclosed mass within a sphere of specified radius is determined using PYNBODY (Pontzen et al. 2013). The second approach is to use the velocity derived from the gravitational potential, $\Phi(R)$, in the midplane of the galaxy as

$$V^{\text{mid}}(R) = \sqrt{R \frac{\partial \Phi(R)}{\partial R}} \Big|_{z=0}, \quad (4)$$

where R is the cylindrical radius, and $z = 0$ denotes the x–y plane, as discussed in Section 4.1. This calculation is also done using PYNBODY.

We determine the maximum velocity of a given RC in two ways. The first is to take the maximum of the total simulated RC. In this case, we define maximum velocities for RCs using spherical symmetry and the midplane potential as V_{\max}^{circ} and V_{\max}^{mid} , respectively. The second is to instead use the maximum velocity for HI-limited RCs within a radius, R_1 , that is consistent with observational limits. Observed low-mass dwarfs have RCs that are sometimes still rising at the detection limit in their last radial bin (Kuzio de Naray et al. 2006; Catinella et al. 2006), implying that the true maximum of their RCs may not be measured (Sales et al. 2017; Ruan et al. 2025). To align our simulation results with observational limits, we calculate the HI gas mass surface density in cylindrical shells from the host center. We define R_1 , the 2D projected size of the HI disk, as the radius where $\Sigma_{\text{HI}} = 1 M_{\odot} \text{ pc}^{-2}$, as motivated by, e.g., Broeils & Rhee (1997) and Wang et al. (2016). Again, we find $R_1 < 15 \text{ kpc}$ for all systems considered in this work. We define maximum velocities for HI-limited RCs using spherical symmetry and the midplane potential as $V_{\max}^{\text{circ+HI}}$ and $V_{\max}^{\text{mid+HI}}$, respectively.

Once the maximum velocity V_{\max} (V_{\max}^{circ} or $V_{\max}^{\text{circ+HI}}$ for spherical symmetry, or V_{\max}^{mid} or $V_{\max}^{\text{mid+HI}}$ for the mid-

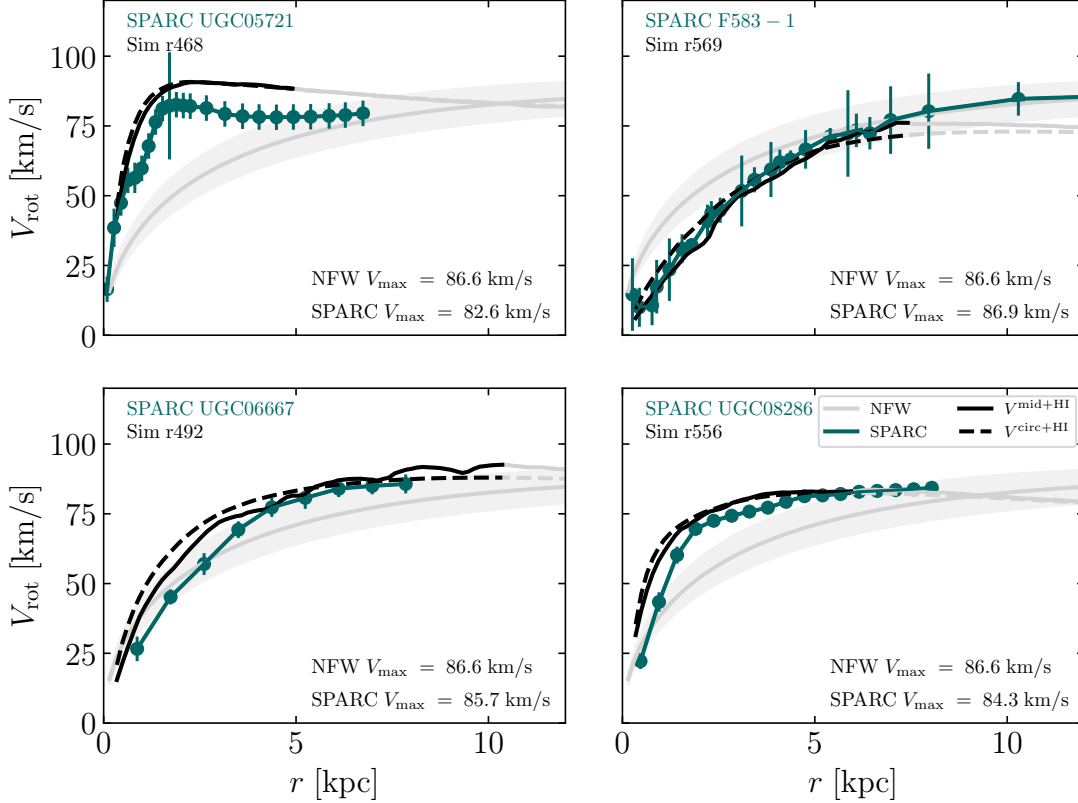


Figure 2. ROTATION CURVES for sample galaxies from SPARC with $V_{\max} \sim 80\text{--}90$ km/s. Full SPARC RCs are shown in dark teal. In each panel, a simulated Massive Dwarf RC with similar shape and V_{\max} to the SPARC RC is shown using spherical symmetry (Equation 3) with a dashed line and from the midplane potential (Equation 4) with a solid line. The full simulated RCs are shown for both cases with dark gray lines (V^{circ} and V^{mid}), and the HI-limited RCs are shown in black ($V^{\text{circ+HI}}$ and $V^{\text{mid+HI}}$). An NFW RC with $V_{\max} \sim 87$ km/s, intermediate to the observed RCs, is shown with scatter in the NFW mass-concentration relationship by the light-gray shaded region. For the two simulations with disks (r492 and r569), the rotation speeds from the midplane potential peak higher and at larger radii than the RCs from the mass-enclosed method. Both the midplane and mass-enclosed RCs exhibit diversity that mimics the observed RCs; the RCs in the upper-left and lower-right panels are more quickly rising than the NFW case. In contrast, the upper right is more slowly rising, and the lower left is in rough agreement with the NFW RC.

plane potential) is determined, a proxy for the central rotation velocity is taken to be

$$V_{\text{fid}} = V_{\text{rot}}(r = r_{\text{fid}}), \quad (5)$$

where $r_{\text{fid}}/\text{kpc} = V_{\max}/(35 \text{ km/s})$ is motivated by Santos-Santos et al. (2020). V_{rot} is the RC obtained using either of the four methods described above (e.g., circ, circ+HI, mid, or mid+HI), which we also indicate in the superscript to V_{fid} . V_{fid} is chosen as the proxy for the central velocity so we can consistently explore RC diversity and compare with previous works (Santos-Santos et al. 2020; Roper et al. 2023; Downing & Oman 2023). While Oman et al. (2015) used 2 kpc, r_{fid} carries the benefit of probing the central parts of a RC, independent of halo mass. V_{fid} is selected so that simulations and most high-resolution HI observations of dwarfs are

able to resolve this radius, allowing for comparison between the two. We explicitly explore the difference between the definitions of maximum and fiducial velocities in Section 5.1.

For the observed RCs from Lelli et al. (2016a), we calculate V_{fid} using the same method as for the simulated curves. In particular, the maximum velocity, V_{\max} is determined for the each galaxy in the SPARC sample identified in Section 3 out to the last observed radial bin. Then, for each SPARC RC we calculate r_{fid} and take V_{fid} to be the rotational velocity in the radial bin closest to that radius.

We limit our analysis to the simulated and observed dwarf galaxies with stellar masses in the range $M_* \sim (5 \times 10^6)\text{--}(1 \times 10^9) M_{\odot}$. We restrict the SPARC sample to galaxies with $V_{\max} < 100$ km/s since that is the

range for most of the simulated galaxies.² By including resolved galaxies outside the virial radius of the main host, we can increase the Massive Dwarf set by seven more galaxies. This results in 47 galaxies from the Marvelous Massive Dwarf zoom suite, 15 galaxies from the Extended Marvelous Massive Dwarf zooms, and 23 from the Marvel suite, for a total of 85 simulated galaxies.

The Massive Dwarf zoom-in simulations include quickly and slowly rising RCs consistent with observations, as demonstrated in Figure 2. In particular, we show examples of four SPARC RCs that exhibit similar behavior at a roughly fixed $V_{\max} \sim 80\text{--}90$ km/s. In each panel, we also show the RCs V^{mid} (solid line) and V^{circ} (dashed line) for a selected simulation. HI-limited RCs ($V^{\text{mid+HI}}$ and $V^{\text{circ+HI}}$) are plotted in black, whereas RCs beyond R_1 are shown in dark gray, suggesting that the RC would not be detected in resolved HI observations at these large radii. In the lowest-mass systems ($V_{\max} \lesssim 60$ km/s), the true V_{\max} can exist at $R_{\max} > R_1$ (see, e.g., Ruan et al. 2025, and the right panel of Figure A1 for examples of such systems). Further, the fiducial radius, r_{fid} , can also be greater than R_1 . In these cases, the ratio $\eta_{\text{rot}} = V_{\text{fid}}/V_{\max}$, a proxy for how fast or slow the RCs rise in the central region, may be larger than the true value if the RC is still rising.

In Figure 2, the RCs derived using the midplane potential peak at larger velocities and at larger radii than the mass-enclosed case, specifically for the systems with disks (r492 and r569). This general shift is consistent with the analytic prediction for RCs of the same mass enclosed in a disk compared to distributed spherically (Binney & Tremaine 2008). The full RCs from SPARC (Lelli et al. 2016a) are plotted in dark teal. The observed diversity contrasts an NFW RC with $V_{\max} \sim 87$ km/s shown in gray, with the shaded band representing the scatter in the mass-concentration relation from Ludlow et al. (2016). The NFW V_{\max} is selected to be intermediate to those of the observed RCs. The self-similar NFW halo density profile is parameterized by the dark matter halo mass (Navarro et al. 1996, 1997) and thus predicts identical RCs for fixed V_{\max} , which is a proxy for the mass of the system. The SPARC RCs in the upper-left and lower-right panels of Figure 2 are more quickly rising than the NFW prediction with $V_{\max} = 86.6$ km/s, but have lower $V_{\max} = 82.6$ km/s and $V_{\max} = 84.3$ km/s, respectively. The most slowly rising SPARC RC in the upper-right panel instead has a very similar $V_{\max} = 86.9$ km/s. The SPARC RC with

the shape closest to NFW has a V_{\max} that is 0.9 km/s lower than the NFW RC.

4.3. Galaxy Sizes

To determine the galaxy sizes, we use PYNBODY to measure the half-light radius of its stars, $r_{1/2}$, in the Johnson K -band using cylindrical coordinates. The K -band is used to mimic SPARC (Lelli et al. 2016a). PYNBODY computes magnitudes of star particles in the K band using the Padova simple stellar populations (Marigo et al. 2008), converts magnitudes to luminosities for all star particles, constructs a galaxy’s total luminosity profile, and identifies the radius that encloses half of that luminosity. To verify our effective radii measurements, we generate mock K -band images of all our galaxies using PYNBODY and measure their Petrosian profiles ($\eta(r)$, Petrosian 1976) with circular apertures using PETROFIT (Geda et al. 2022). The Petrosian radius (r_p) is defined as the radius at which the profile reaches a predefined Petrosian index (η_p , where $\eta(r_p) = \eta_p$). The total flux radius is then calculated by multiplying the Petrosian radius by a constant ($r_{\text{total}} = \epsilon_p \cdot r_p$). Measurements using SDSS parameters ($\eta_p = 0.2$ and $\epsilon_p = 2$, Strauss et al. 2002) yield nearly identical values between Petrosian half-light radii (i.e., $L(\leq r_{0.5}) = 0.5L(\leq r_{\text{total}})$, where L is the projected luminosity) and our PYNBODY-derived effective radii. Furthermore, for galaxies whose light profiles are well described by a single component Sérsic model (Sérsic 1963), we fit 2D Sérsic profiles using PETROFIT. The effective radii parameters of the fitted single-component Sérsic models are within 0.3 kpc of our effective radii measurements.

5. DIVERSITY OF ROTATION CURVES

5.1. Rotation curve shapes

We quantify the diversity of the simulated RC shapes by comparing the fiducial velocities, V_{fid} , to the maximum circular velocities, V_{\max} , in Figure 3. RCs derived with a spherical enclosed mass (Equation 3) are plotted in the top row and those using the midplane calculation (Equation 4) are in the bottom row. The left column takes the maximum of the RCs out to R_1 , while the right column uses the maximum of the total simulated RC. In each panel, the SPARC data points are shown as gray diamonds, Marvel galaxies are the teal squares, and the Massive Dwarf zooms are the purple circles. The 1 : 1 line is shown in dashed black, and the NFW prediction is shown by the gray shaded region. For a given V_{\max} , the associated NFW RC is obtained by sampling the concentration from the Ludlow et al. (2016) relation; the bands in the figure correspond to the root-mean-

² One simulated galaxy with $V_{\max} > 100$ km/s at $z = 0$ has $V_{\max} < 100$ km/s at $z = 0.1$, after which it underwent a major merger.

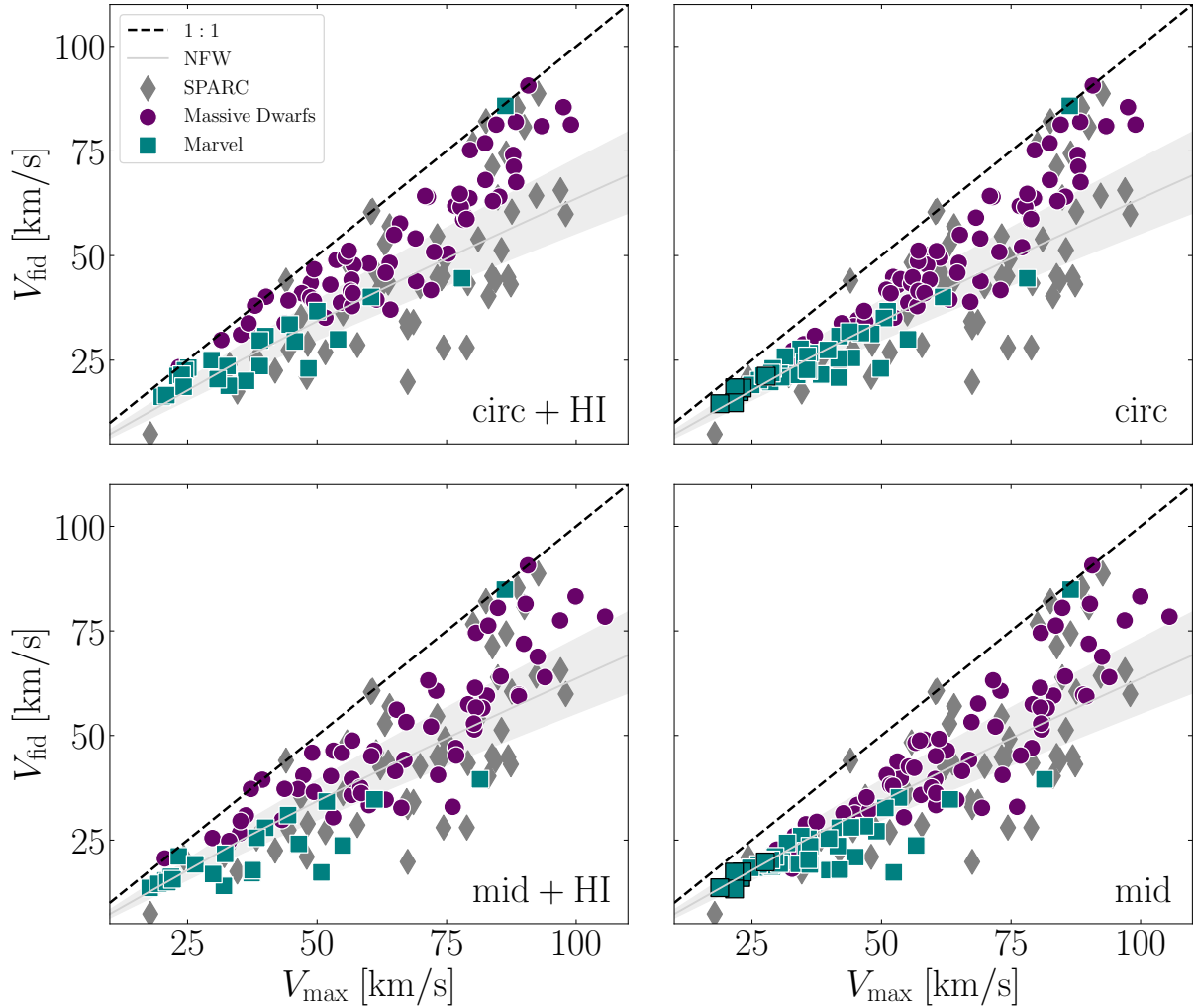


Figure 3. FIDUCIAL VELOCITY VERSUS MAXIMUM CIRCULAR VELOCITY for SPARC in gray diamonds, the Massive Dwarf zooms in purple circles, and the Marvel dwarfs in teal squares. The NFW prediction is shown by the gray line with the shaded region representing the root-mean-square scatter in the mass-concentration relation reported in Ludlow et al. (2016). The dashed black 1 : 1 line represents where V_{fid} is equal to V_{max} . The results correspond to the following velocities $V^{\text{circ+HI}}$ (upper left), V^{circ} (upper right), $V^{\text{mid+HI}}$ (lower left), and V^{mid} (lower right). For some of the lowest-mass Marvel galaxies, there is limited HI and $R_1 < r_{\text{conv}}$; we mark these galaxies with black outlines on the teal squares to denote that they are HI-limited and excluded from the left panels. A larger spread in inner velocities at r_{fid} at a fixed V_{max} is predicted for the midplane potential compared to the spherical case. RCs that are more quickly and more slowly rising than NFW are predicted with the midplane method down to $V_{\text{max}}^{\text{mid+HI}} \sim 50$ km/s in the Massive Dwarf zooms.

square scatter from the concentration uncertainty. For an NFW RC with a given V_{max} , the associated r_{fid} is derived, and then the V_{fid} is calculated using Equation 5. We denote low-mass objects that do not have sufficient HI outside of the resolved region (r_{conv}) with black outlines. These objects are not shown in the cases where V_{max} is determined out to R_1 (left column).

To start, we compare the different RC methods against each other, starting with the circ and mid methods. For the case of circ and circ+HI (top row), most

simulated galaxy RCs have a V_{fid} that is above or in agreement with the NFW prediction at a given V_{max} . The mid and mid+HI cases (bottom row) both exhibit a lower median and more extended spread in V_{fid} , for given V_{max} , than seen in the top row. For example, for halos with $V_{\text{max}} = 60\text{--}80$ km/s, the 16-50-84th percentiles for V_{fid} are $56.3_{48.1}^{61.8}$ km/s and $45.2_{34.1}^{56.7}$ km/s for circ+HI and mid+HI, respectively.

In Appendix A, we examine the shifts for individual galaxies when changing from circ+HI to mid+HI. The

V_{\max} [km/s]	SPARC V_{fid} [km/s]	Massive Dwarfs $V_{\text{fid}}^{\text{mid+HI}}$ [km/s]	Marvel $V_{\text{fid}}^{\text{mid+HI}}$ [km/s]
20–40	21.4 $^{24.4}_{19.6}$ (5)	28.1 $^{36.5}_{24.9}$ (8)	17.1 $^{22.0}_{15.3}$ (13)
40–60	28.8 $^{40.6}_{24.4}$ (10)	37.4 $^{45.9}_{36.0}$ (16)	24.1 $^{32.1}_{21.4}$ (5)
60–80	44.1 $^{54.5}_{33.0}$ (20)	45.2 $^{56.7}_{34.1}$ (17)	34.7 (1)
80–100	63.9 $^{80.9}_{44.7}$ (19)	64.1 $^{80.6}_{56.7}$ (19)	62.2 $^{77.6}_{46.8}$ (2)

Table 1. Binned RC shape statistics for SPARC and simulated galaxies. V_{fid} statistics are derived for four evenly spaced V_{\max} bins between 20–100 km/s. In each column, the 16-50-84th percentiles are provided for the specified sample, with the number of galaxies in that bin indicated in parentheses. For the simulated galaxies, $V_{\max}^{\text{mid+HI}}$ and $V_{\text{fid}}^{\text{mid+HI}}$ values are reported. The Massive Dwarfs and SPARC have similar 16-50-84th percentiles between $V_{\max} = 60$ –80 km/s and similar 50-84th percentiles between $V_{\max} = 80$ –100 km/s, but the Massive Dwarfs have a higher 16th percentile in this range, indicating the more slowly rising RCs are missing in this bin. In the two lowest V_{\max} bins, neither simulation suite independently matches the SPARC data well.

left panel of Figure A1 shows the shift between the upper and lower left panels of Figure 3. For the more massive galaxies, i.e., with $V_{\max} \gtrsim 60$ km/s, the largest shifts occur for systems with disks (see Appendix A for disk definition). These galaxies both shift to higher V_{\max} and also lower V_{fid} . As mentioned above, a disk potential causes the RC to peak at larger velocities and at larger radii than a spherical potential (Binney & Tremaine 2008). Changing from the circ to mid method naturally captures the change in potential in disk-dominated galaxies. At lower V_{\max} , shifts can occur in systems without disks. Previous works have shown that low-mass galaxies have bursty star formation with feedback that drives the galaxies out of equilibrium (e.g., Read et al. 2016a; El-Badry et al. 2017; Verbeke et al. 2017; Downing & Oman 2023; Sands et al. 2024). If galaxies are undergoing outflows from the midplane, this will reduce the measurement using the midplane potential relative to the mass enclosed in spherical shells. Since outflows are centralized (e.g., Brook et al. 2011), this will be more likely to reduce V_{fid} than V_{\max} , consistent with the shifts seen in the lower-mass galaxies in Figure A1. In summary, while the specific mechanism that causes the shift differs across V_{\max} , in both cases the shift is due to deviation from spherical symmetry.

Next, we examine the shifts in RC shape due to measuring V_{\max} within R_1 instead of using the full V_{\max} determined from the simulations. In the HI-limited case (left panels of Figure 3), there are a number of systems where $V_{\max} \sim V_{\text{fid}}$, falling close to the 1 : 1 line. These same galaxies do not lie near the 1 : 1 line when measuring the full V_{\max} , instead agreeing well with the NFW prediction. The right panel of Figure A1 examines this shift, which occurs predominantly in low- V_{\max} galaxies. In such low-mass systems, the full RCs are still rising at R_1 . RCs that are still rising in the last HI-limited radial bin are also observed (e.g., McQuinn et al.

2022), and indeed similar objects exist in the SPARC sample. In these systems, by definition V_{\max} is measured at a smaller radius in the HI-limited case than in the full case, resulting in lower V_{\max} . Because r_{fid} is determined by V_{\max} , V_{fid} is also measured at a smaller radius. Figure A1 shows that the shift tends to be larger in V_{\max} than in V_{fid} , but the overall effect is that V_{\max} and V_{fid} are measured much closer together in radius, and the overall galaxy shifts toward the 1 : 1 line.

Throughout the rest of the work, we use the mid+HI method because we expect it to most closely mimic mock observations, i.e., capturing the impact of disk potentials, dynamical disequilibrium, and the observational R_1 limit. Hence, it is likely the method that best mimics the SPARC data. However, there are many other effects that can change the observed RCs of galaxies that will not be captured by any of the measurement methods, including mid+HI. We refer the reader to Section 7.1 for a more in-depth discussion.

When the mid+HI method is used, we find a broad range of diversity in the $V_{\text{fid}} - V_{\max}$ plane, with galaxies that both rise more slowly and more quickly than NFW. To quantify the spread in V_{fid} , we split the SPARC and simulation samples into four evenly spaced V_{\max} bins between 20–100 km/s and quantify the median V_{fid} and 16-84th percentiles in each. The results are summarized in Table 1. We note that this method is not perfect as each sample has a different selection function (for the simulation suites the selection criteria is discussed in Section 2), however it aids in comparing the samples. This table helps us explore how well either simulation set matches the observational SPARC data and whether the two simulation sets produce consistent predictions for RC shape at fixed V_{\max} . Note that we do not comment on bins that are statistically-limited, with fewer than five galaxies in them.

In the upper $V_{\max} = 80\text{--}100$ km/s bin, the median and upper percentile for SPARC and the Massive Dwarf zooms agree well; however, the lower percentile for SPARC is ~ 10 km/s smaller. This is visually evident in Figure 3 as we do not reproduce a few of the most slowly rising objects in SPARC between $V_{\max} \sim 80\text{--}100$ km/s. As discussed in Section 7.1, these discrepancies can potentially be explained by effects like non-circular motion in observed RCs, which tend to lower observed rotation velocities.

In the $V_{\max} = 60\text{--}80$ km/s bin, the Massive Dwarf zooms agree very well with SPARC. In particular, SPARC has $V_{\text{fid}} = 44.1_{-33.0}^{+54.5}$, while the mid+HI case has a slightly higher median but similar percentile range with $V_{\text{fid}}^{\text{mid+HI}} = 45.2_{-34.1}^{+56.7}$ km/s. The Marvel zoom volumes only have a single object in this V_{\max} range, so we cannot derive statistical results.

In the two lowest V_{\max} bins, neither simulation suite independently matches the SPARC data well. The Massive Dwarf zooms have higher medians than SPARC, with the lower quartile not encompassing the SPARC median. The Marvel zoom volumes have lower median compared to SPARC, but the upper quartile does a better job of encompassing the median SPARC V_{fid} values.

Differences between the two simulation suites could arise from their different feedback prescriptions. The Massive Dwarf zooms are run with superbubble feedback, whereas the Marvel zoom volumes are run with blastwave feedback. In Figure B1 of Appendix B, we compare the diversity of RCs for galaxies in the Marvel Storm zoom volume, run with both blastwave and superbubble feedback, using $V_{\max}^{\text{mid+HI}}$. There is a preference towards larger $V_{\max}^{\text{mid+HI}}$ for a given galaxy in the runs with superbubble feedback. Azartash-Namin et al. (2024) compared galaxy and halo properties in superbubble versus blastwave feedback. They found no change in stellar size between the two feedback models, but they did find that the simulations with superbubble feedback have preferentially higher halo masses compared to their blastwave counterparts (see their Figure 1). We postulate that this preference for higher halo masses is translated into larger $V_{\max}^{\text{mid+HI}}$ in superbubble compared to blastwave feedback in the Storm simulations.

The impact of the higher $V_{\max}^{\text{mid+HI}}$ in the superbubble runs on the diversity of RCs is not immediately obvious. Most of the galaxies in Figure B1 move mostly along the NFW expectation when changing from blastwave to superbubble feedback. This is because $V_{\text{fid}}^{\text{mid+HI}}$ tends to be slightly higher as well. However, the most massive galaxy in that set makes it clear that an increase in V_{\max} can introduce more diversity if V_{fid} remains ap-

proximately constant. At the moment, it is not conclusive whether the choice of feedback model impacts the diversity of RCs, or in what direction.

For a fixed V_{\max} in the midplane case, we find values of V_{fid} both above and below the NFW prediction. This is in contrast to other simulation suites such as NIHAO, which only show slowly rising RCs when using the midplane method in the V_{\max} range considered in this work (Santos-Santos et al. 2018). Similarly, EAGLE simulations run with a high density threshold for star formation also struggled to produce the most quickly rising RCs (Santos-Santos et al. 2020). In both the NIHAO and EAGLE simulations that preferentially made slowly rising RCs, baryonic feedback also induced dark matter density cores in the central galaxy. In Appendix C, we show that the Marvel and Massive Dwarf simulations can produce cored dark matter density profiles, i.e., these are the first simulations to simultaneously make dark matter cores while also producing quickly rising RCs. In the next section we explore the relation between baryonic distribution and RCs in these new simulations.

5.2. The influence of baryons on diversity of rotation curves

How baryons contribute to RC shape, and whether the shapes of RCs are correlated with baryonic surface densities, are debated questions. Ren et al. (2019) showed that the shape of SPARC RCs correlates with surface brightness, at least for galaxies in their highest V_{\max} bin, 79–91 km/s. However, Santos-Santos et al. (2020) demonstrated that dwarf galaxies show a broad range in RC shape at a given baryonic surface density, concluding that RC shape and surface brightness are not correlated, in contrast to Ren et al. (2019). In this subsection, we investigate the relation between baryonic distribution and RC shape in the Marvel and Massive Dwarf galaxy suites.

To quantify the connection between RC shape and baryonic distribution in our simulations, we define baryonic surface densities using the baryonic half-mass radius. Following Section 4.3, we calculate the cumulative luminosity profile for the stars and then convert to mass using a mass-to-light ratio of $\Upsilon_* = M_*/L_* = 0.5 M_\odot/L_\odot$ (McGaugh & Schombert 2014; Lelli et al. 2016a,b). The value of $\Upsilon_* \approx 0.5 M_\odot/L_\odot$ was found to minimize the scatter around the baryonic Tully-Fisher relationship (Lelli et al. 2016b) and to be consistent with stellar population synthesis models with standard initial mass functions (McGaugh & Schombert 2014). Mass profiles are calculated this way instead of taking the stellar mass directly from the simulations to

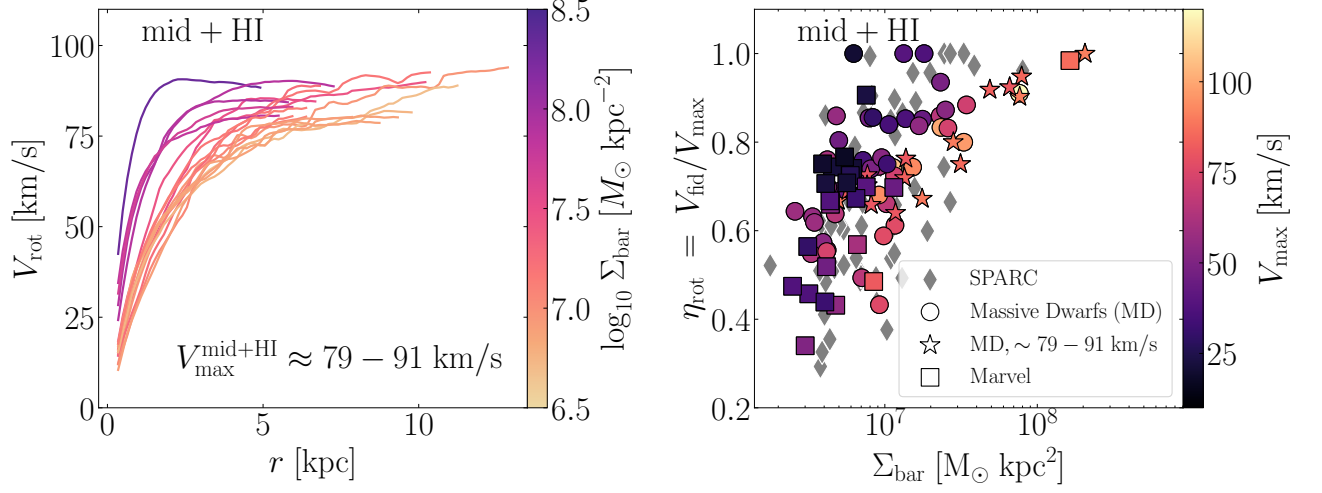


Figure 4. Left: MIDPLANE RCs COLORED BY BARYONIC SURFACE DENSITY. The RCs are cut off at R_1 and are chosen in a V_{\max} range that matches with Ren et al. (2019). The HI-limited midplane method is used to calculate V_{fid} and V_{\max} . The most quickly rising RCs (violet) have higher surface densities, whereas the more slowly rotating RCs (orange) have lower surface densities. This trend is consistent with observed RCs in the same V_{\max} range (Lelli et al. 2016a). **Right:** η_{rot} versus Σ_{bar} , with simulated galaxies colored by V_{\max} and SPARC data in gray. In the simulated and observed galaxies, higher-mass systems have higher baryonic surface densities and have RCs that tend to rise more quickly. There is large scatter in η_{rot} at lower Σ_{bar} . Systems with $V_{\max} \sim 79\text{--}91$ km/s that appear in the left panel are highlighted with star markers.

mimic the observational procedure. The enclosed HI gas mass profile is calculated out to R_1 and multiplied by 1.4 to account for helium and metals in the gas phase (Arnett 1996; Bradford et al. 2016). Consistent with Lelli et al. (2016a), we do not account for the contribution of molecular gas because such data is not available for most SPARC galaxies and molecules are expected to be subdominant compared to stars and atomic gas (Simon et al. 2003; Frank et al. 2016). We find that $R_1 > r_{1/2}$, in agreement with SPARC (Lelli et al. 2016a). The simulated stellar and gas enclosed mass profiles are added, and we find the radius $r_{1/2,\text{bar}}$ where half of the total baryonic mass, $M_{\text{bar}} = M_* + 1.4M_{\text{HI}}$, is enclosed. Then, we calculate the baryonic surface density as $\Sigma_{\text{bar}} = M_{\text{bar}}/2\pi r_{1/2,\text{bar}}^2$, consistent with Santos-Santos et al. (2020).

To calculate the baryonic surface densities for SPARC galaxies, we derive gravitational baryonic contributions to the RCs, $V_{\text{bar}}^2(r) = V_{\text{gas}}^2(r) + \Upsilon_* V_*^2(r)$ from published mass models (Lelli et al. 2016a). We note that for the SPARC galaxies considered in this study, there are no stellar bulge contributions to V_* . The baryonic half-mass radii are derived using spherical symmetry with $M_{\text{bar}}(< r) = rV_{\text{bar}}^2(r)/G$.

To probe the connection between baryonic surface density and RC shape, the left panel of Figure 4 examines the set of galaxies with $V_{\text{max}}^{\text{mid+HI}} = 79\text{--}91$ km/s

to match Ren et al. (2019).³ The R_1 cut causes each RC to end at a different radius, as for observed galaxies. For this range of $V_{\text{max}}^{\text{mid+HI}}$, the most quickly rising RCs have high baryonic surface densities; baryons dominate the central potentials in these systems (see for example density profiles for r488, r502, r468, r555 in Figure C1). On the other hand, the more slowly rising RCs have low baryonic surface densities. However, this trend does not exist for lower V_{\max} values than those shown here, in agreement with Santos-Santos et al. (2020).

The parameter

$$\eta_{\text{rot}} = V_{\text{fid}}/V_{\text{max}} \quad (6)$$

is a proxy for the shape of a RC, as it compares the central velocity with its maximum (Santos-Santos et al. 2020). For the NFW model, η_{rot} increases slightly with decreasing V_{\max} . As a benchmark, note that galaxies with $\eta_{\text{rot}} \gtrsim 0.65\text{--}0.75$ are more quickly rising in their central regions than the corresponding NFW prediction (with scatter from the mass-concentration relation), and galaxies with $\eta_{\text{rot}} \lesssim 0.55$ are more slowly rising. The right panel of Figure 4 shows the relationship between η_{rot} , the baryonic surface density Σ_{bar} , and $V_{\text{max}}^{\text{HI+mid}}$ for

³ We do not color by surface brightness as in Ren et al. (2019), but the baryonic surface density and brightness should be consistent up to a scaling factor for a fixed mass-to-light ratio, as advocated for in Lelli et al. (2016a).

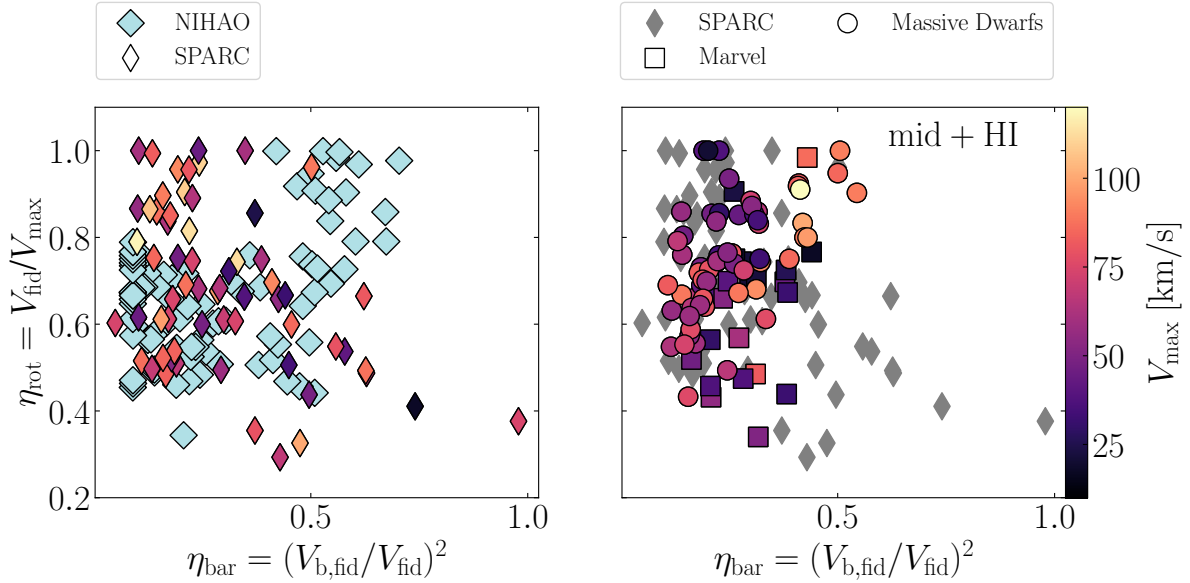


Figure 5. η_{rot} VERSUS BARYON MASS FRACTION WITHIN r_{fid} , colored by V_{max} , for **Left:** SPARC data in thin colored diamonds with mass modeling from Lelli et al. (2016a). Objects in the upper-left region have low central baryon mass fractions, but are still more quickly rising in their central regions than the NFW prediction. Previous CDM and baryon simulations have struggled to reproduce these objects. This is demonstrated for NIHAO data (from Santos-Santos et al. 2020) in light blue diamonds, including galaxies with $V_{\text{max}} > 100$ km/s and measured using enclosed mass. **Right:** The Massive Dwarf zooms in circles and the Marvel sample in squares, using the midplane potential to calculate velocities. Most of the simulated galaxies have $\eta_{\text{bar}} \lesssim 0.5$. There is a significant spread in η_{rot} in this region, including some systems with $\eta_{\text{rot}} \gtrsim 0.75$, higher than the NFW prediction.

the full simulated and observed samples. The galaxies shown in the left panel are indicated as stars, making it obvious that there is a clear trend between η_{rot} and baryonic surface density for galaxies with $V_{\text{max}}^{\text{mid+HI}} = 79\text{--}91$ km/s. In the simulations, galaxies with higher baryonic surface density tend to be more quickly rising, i.e., have larger η_{rot} values. However, there is significant scatter for galaxies with $\Sigma_{\text{bar}} < 10^7 M_{\odot} \text{ kpc}^{-2}$, showing that the correlation with baryonic surface density evident in the left panel does not hold at lower V_{max} values.

The simulated galaxies with the most quickly rising RCs (i.e., those with high η_{rot}) bracket the range of surface densities in the observations, although the (two) highest-mass simulated galaxies have higher surface densities than SPARC. On the other hand, at every $\Sigma_{\text{bar}} < 3 \times 10^7 M_{\odot} \text{ kpc}^{-2}$, there is a subset of SPARC galaxies that are more slowly rising than the simulations. These SPARC systems may be influenced by non-circular motions (Read et al. 2016b; Downing & Oman 2023) or inclination (Roper et al. 2023), making them appear more slowly rising. We discuss these effects further in Section 7.1.

In addition to surface densities, we examine the relationship between central baryonic mass fraction and RC shape using mass models for the SPARC data (Lelli et al. 2016a). Assuming spherical symmetry, the cen-

tral baryonic mass fraction within r_{fid} can be quantified using RCs with

$$\eta_{\text{bar}} \equiv (V_{\text{b,fid}}/V_{\text{fid}})^2, \quad (7)$$

where $V_{\text{b,fid}}$ is the fiducial velocity of the baryonic RCs. Santos-Santos et al. (2020) used this definition and η_{rot} to explore how the central baryon mass fraction relates to the shapes of RCs, as in Figure 5. The SPARC data are indicated by the diamonds in both panels, colored by V_{max} for the left and indicated in gray for the right. The NIHAO galaxies extracted from Santos-Santos et al. (2020) are shown in light blue on the left. The Massive Dwarf galaxies (circles) and Marvel dwarfs (squares) are colored by their $V_{\text{max}}^{\text{mid+HI}}$ on the right panel.

For galaxies with lower baryonic mass fractions ($\eta_{\text{bar}} \lesssim 0.5$), we find simulated galaxies with a spread in RC shape η_{rot} that includes objects that rise more quickly than the NFW prediction. This is in contrast to the NIHAO results shown in Figure 5—and also for EAGLE and APOSTLE (Santos-Santos et al. 2020), which are not shown. In particular, observed dwarfs in the upper-left of each panel in Figure 5, which are more quickly rising than NFW ($\eta_{\text{rot}} \gtrsim 0.75$) and have low η_{bar} , are absent in NIHAO. However, the Massive Dwarf zoom galaxies occupy this space. These simulated systems are influenced by the HI-limited velocity measurement method, pushing them closer the 1 : 1 line, as

discussed in Section 5.1 and shown in Appendix A. Although there are simulated galaxies in the upper left region, the higher V_{\max} SPARC systems in this region are still missing from our sample. Roper et al. (2023) examined two simulated galaxies and showed that systems with high η_{rot} and low η_{bar} could be found in mock HI RCs along special viewing angles, an effect that we neglect here.

Other SPARC galaxies of interest have RCs that are slowly rising (low η_{rot}), but have large central baryonic mass fractions (high η_{bar}). These are the SPARC galaxies in the lower-right corner of the $\eta_{\text{rot}} - \eta_{\text{bar}}$ plane in Figure 5. They are the same SPARC objects that are missing from the Massive Dwarf and Marvel simulations below the NFW prediction in Figure 3 and the missing slowly rising objects in Figure 4. NIHAO and EAGLE simulations that create dark matter cores do a better job producing slowly rising objects with larger baryon mass fractions. However, even in NIHAO, a fraction of these SPARC systems are still missing, as shown in the left panel of Figure 5. It is possible that all of the simulated galaxies, including those presented here, have mass-loading factors too high relative to real galaxies (e.g., Collins & Read 2022). Indeed, as we explore below, we believe the NIHAO simulations have stronger feedback than our fiducial runs, preventing them from making both the steeply rising galaxies and compact galaxies. Alternatively, Santos-Santos et al. (2018), Roper et al. (2023), and Oman et al. (2019) suggest that the observed galaxies in the lower-right corner may be affected by non-circular motion.

In this subsection, we explored how and if baryons impact the diversity of RC shapes. Our simulations are able to produce quickly rising RCs with low central baryon mass fractions that other simulations have had difficulty producing. We think the reason is partially due to the inclusion of the R_1 cut on RCs, used to mimic observations. Alternatively, η_{bar} may be biased by assuming spherical symmetry rather than accounting for a disk geometry. However, there is a subset of slowly-rising SPARC galaxies that we do not reproduce, and we see this in a variety of different galaxy property planes. Moreover, these galaxies tend to have non-negligible contributions of baryons. While these objects may be better produced for stronger feedback models as in EAGLE and NIHAO (Santos-Santos et al. 2020), we suspect they may instead be influenced by non-circular motions, as suggested by Santos-Santos et al. (2018); Oman et al. (2019); Roper et al. (2023), because the strong feedback scenario prevents the formation of compact galaxies found in SPARC (e.g., Jiang et al. 2019). We examine the role of feedback in Section 6.

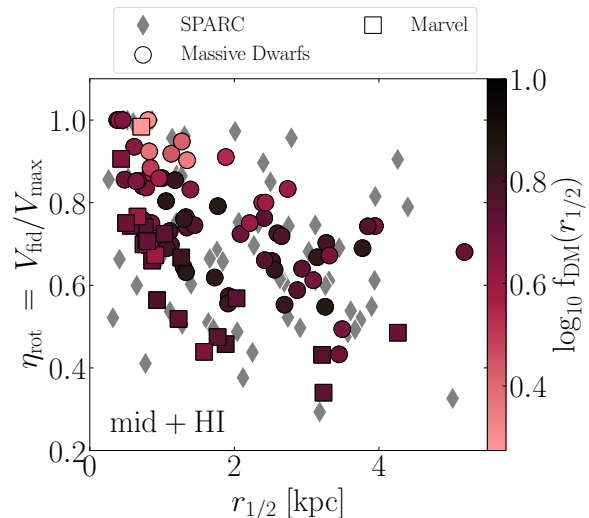


Figure 6. η_{rot} VERSUS HALF-LIGHT RADIUS, $r_{1/2}$, COLORED BY DARK MATTER MASS FRACTION WITHIN $r_{1/2}$ FOR OUR SIMULATED SAMPLE AT $z = 0$. THE OBJECTS THAT ARE QUICKLY RISING HAVE SMALLER HALF-LIGHT RADII AND $f_{\text{DM}}(r_{1/2})$, MEANING THEY ARE BARYON DOMINATED. HOWEVER, THERE ARE ALSO OBJECTS AT LOWER η_{rot} THAT HAVE SMALLER SIZES BECAUSE THEY ARE LESS MASSIVE. THE CORRELATION BETWEEN η_{rot} AND $r_{1/2}$ IS CONSISTENT WITH MOST OF THE SPARC OBSERVATIONS.

5.3. Diversity in the size- M_* plane

Beyond the diversity in RCs, dwarf galaxies are observed to have a spread in size at a given M_* (Carlsten et al. 2021). In Section 5.2, we found that RCs exhibit a diversity of baryonic surface densities, which may be linked to the diversity of the size- M_* relationship. Figure 6 examines the relationship between η_{rot} versus $r_{1/2}$ for the Massive Dwarf and Marvel galaxies. Each simulated galaxy is colored by its dark matter mass fraction within $r_{1/2}$, f_{DM} . Although there is scatter, objects with smaller $r_{1/2}$ tend to have higher η_{rot} and lower f_{DM} , i.e., simulated galaxies with quickly rising RCs (high η_{rot}) are also the most compact. However, the converse is not true. Simulated galaxies with slowly rising RCs (low η_{rot}) instead show a range of sizes. This is due to the size- M_* relationship and its scatter at a given mass. For fixed V_{\max} (e.g., galaxy mass), η_{rot} can extend over the full range from $\sim 0.3-1$ (see Figure 5) and is also inversely correlated with $r_{1/2}$. Moreover, given the size- M_* relation, galaxies with larger stellar masses typically have larger median sizes. This naturally leads to the result that all galaxies (from small to large V_{\max}) converge towards $\eta_{\text{rot}} \sim 1$ as $r_{1/2}$ decreases. Instead, when $\eta_{\text{rot}} \sim 0.4$, the lower-mass (higher-mass) galaxies will populate the lower (upper)-end of $r_{1/2}$ values.

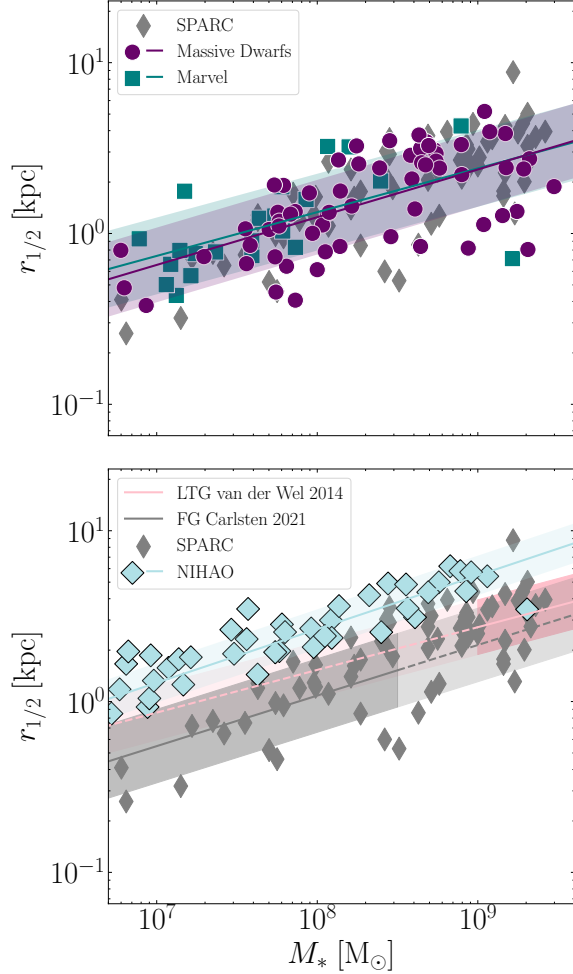


Figure 7. $r_{1/2}$ VERSUS M_* for **Top:** Massive Dwarf zooms in circles, the Marvel dwarfs in squares, and SPARC in gray diamonds. Power-law fits are shown for the Massive Dwarfs and Marvel in purple and teal, respectively. The Massive Dwarfs and the Marvel galaxies cover the same area as SPARC. **Bottom:** The late-type-galaxy (LTG) size- M_* relation for normal-size galaxies is shown in the pink shaded region for $M_* > 10^9 M_\odot$ (van der Wel et al. 2011). The field size- M_* relationship is shown by the gray line and shaded region, corresponding to $1-\sigma$ scatter, for $M_* < 10^{8.5} M_\odot$ (Carlsten et al. 2021). The extrapolation of each observed relation is shown by a dashed line. $r_{1/2}$ versus M_* for the NIHAO simulation suite is shown in light blue diamonds (Jiang et al. 2019). The NIHAO simulated suite size- M_* relationship is offset from the SPARC galaxies, as well as the fitted size- M_* relationships, particularly below $M_* \sim 10^9 M_\odot$.

The net result is significant scatter in galaxy sizes when $\eta_{\text{rot}} \lesssim 0.6$. Except for a few objects at the extremes, the simulated sample covers a similar area in the $\eta_{\text{rot}} - r_{1/2}$ plane to the SPARC sample, indicated by the gray diamonds.

In addition to struggling to reproduce the diversity of RCs, previous simulation suites have struggled to produce size- M_* relationships consistent with observations. In dwarf galaxies, compact and extended galaxies are observed at a given stellar mass whereas most simulations with strong feedback only produce the most diffuse objects. We examine the size- M_* relationship in the Marvel and Massive Dwarf simulations in Figure 7. In the top panel, the SPARC galaxies are shown in gray diamonds, with the Marvel galaxies in teal squares, and the Massive Dwarf zooms in purple circles. The size is given in terms of the half-light radius, as outlined in Section 4.3. The bottom panel shows SPARC galaxies in gray diamonds and galaxies from the NIHAO simulation suite extracted from Jiang et al. (2019) as light blue diamonds. The observed trend for late-type galaxies from van der Wel et al. (2011) is shown by the pink solid line, which changes to dashed below $M_* \lesssim 10^9 M_\odot$ where it is extrapolated. The pink shaded region indicates the 68% containment interval of scatter in the observed relation. We additionally show the observation from ELVES dwarf galaxies with the field size- M_* relationship in gray for $M_* < 10^{8.5} M_\odot$ from Carlsten et al. (2021). The dashed gray line denotes the extrapolation of the relationship above $M_* \gtrsim 10^{8.5} M_\odot$. van der Wel et al. (2011) examines larger-mass galaxies with $M_* > 10^9 M_\odot$ whereas Carlsten et al. (2021) focuses on the dwarf regime with $M_* \lesssim 10^{8.5} M_\odot$ and each are extrapolated to cover the full range of M_* considered in this work. The Carlsten et al. (2021) size- M_* relationship overlaps with the SPARC galaxies, but the relationship inferred at higher masses is offset below the SPARC data.

At $M_* \lesssim 10^9 M_\odot$, the Massive Dwarf zooms and the Marvel galaxies cover a similar area as the SPARC galaxies in the size- M_* plane (upper panel of Figure 7). In contrast, the NIHAO galaxies are offset from the observed relations (lower panel). A similar offset is noted for FIRE (though see Klein et al. 2024) and galaxies from Lupi et al. (2017) in Jiang et al. (2019). We fit a power law to the size- M_* relationship as

$$\log_{10}(r_{1/2}/\text{kpc}) = a + b \log_{10} \left(\frac{M_*}{5 \times 10^6 M_\odot} \right) \quad (8)$$

and calculate the scatter σ as the standard deviation of the simulated data from the best-fit line. For the Massive Dwarfs, $a = -0.268$, $b = 0.279$, and $\sigma = 0.218$. Marvel has a slightly shallower slope and larger scatter with $a = -0.208$, $b = 0.256$, and $\sigma = 0.225$. Both Marvel and Massive Dwarfs are in fair agreement with

Carlsten et al. (2021)⁴ which reports $a = -0.347$, $b = 0.296$, $\sigma = 0.215$. However, the NIHAO relationship has less scatter and is offset with $a = 0.015$, $b = 0.314$, and $\sigma = 0.116$. For intuition on a , note that the $M_* = 5 \times 10^6 M_\odot$ intercept is 0.450 kpc for the Carlsten et al. (2021) field galaxy relationship, compared to 0.540 kpc for the Massive Dwarfs, and 1.036 kpc for NIHAO.

Previous galaxy formation models in CDM with baryons have failed to produce compact objects below $M_* \sim 10^9 M_\odot$ (Jiang et al. 2019; Sales et al. 2022). Given the relation we have found here between steeply rising RCs and compact sizes (Figure 6), it seems that a failure to make compact objects may be tied to why previous simulations have failed to reproduce the most quickly rising RCs (Santos-Santos et al. 2018, 2020). We do find objects as compact and extended as the SPARC galaxies across stellar mass in both the Marvel and Massive Dwarf galaxies.

In future work, we will examine the origin of the varying sizes in the simulated dwarfs (Geda et al. 2025). Here, we restrict our analysis to understanding why previous simulations may not have made compact galaxies. We explore this in the next section.

6. THE ROLE OF SUBGRID PHYSICS

The simulations studied in this work include both compact and extended objects, in better agreement with observations than previous numerical studies. For example, the sample of galaxies at $M_* \lesssim 10^9 M_\odot$ in NIHAO and FIRE is offset from the observed size- M_* relationship, with all of the objects being more extended (Jiang et al. 2019). This section performs a detailed comparison of the Massive Dwarf zoom-in simulations to NIHAO, seeking to identify the source of this difference. We focus on NIHAO because it was run with GASOLINE2 (Wadsley et al. 2017), which has a similar hydrodynamics code to CHANGA, allowing us to rerun galaxies with different parameter choices to determine their impact.

To perform this comparison, we run controlled experiments on two galaxies, r556 and r618, that are more compact than the $1-\sigma$ interval of the observed field galaxy size- M_* relationship found in Carlsten et al. (2021). We attempt to mitigate numerical butterfly effects by ensuring the two galaxies also have quiescent merger histories after $z \sim 2$ (Genel et al. 2019; Keller et al. 2019). Keller et al. (2019) showed that major

mergers (1 : 1) can significantly alter stellar masses in simulations with the same ICs and subgrid physics, just re-run many times. Because Keller et al. (2019) found that sizes are stable to numerical chaos, but morphologies are not, we only focus on differences in size. Beyond this, they showed that galaxies with higher surface densities, like r556 and r618, tended to be more immune to galactic chaos. While we attempt to mitigate these non-linear effects, they may still impact differences in size and mass as the subgrid physics is varied below.

Table 2 summarizes the six different subgrid physics variations that are considered. The Tests are performed in steps from the fiducial model to a subgrid model more closely resembling NIHAO. The fiducial model (see Section 2.2) differs from the NIHAO subgrid model (detailed in Section 2.3) in star formation, feedback, and resolution.

Figure 8 shows the differences in UVI images due to the subgrid physics variations. The top row shows variations of simulation r556, and the bottom row shows r618. The first column of Figure 8 shows the fiducial model, designated Test 1 in Table 2. Relative to the full set of galaxies in Figure 1, it is visually apparent that these two are some of the most compact in the Massive Dwarf sample. Figure 9 quantifies the shifts in the size- M_* plane associated with each subgrid variation with r556 in magenta and r618 in black, each numbered with the associated Test listed in Table 2. Our goal is to understand whether changes that bring the subgrid model in closer alignment to that used by NIHAO also change the compactness of these systems.

6.1. Black Holes

First, we rerun the fiducial model without BHs. This is done because the NIHAO simulations we compare to do not include BHs. In Milky Way-mass galaxies, the absence of a BH should increase star formation, altering M_* (Tremmel et al. 2017); however, the expectation for how intermediate-mass BHs impact dwarf galaxies is less well studied. As was discussed in Section 2.2, Bellovary et al. (2019) found little BH accretion in the Marvel galaxies, which suggests that there should be little change to $r_{1/2}$ and M_* when BHs are removed. The second column in Figure 8 shows the result of Test 2, in which the only change is to remove BHs from the fiducial model. The $r_{1/2}$ remains roughly constant in r618, but increases by roughly 50% in r556 (see Figure 9). In addition to the two galaxies shown here, we also explored a larger set of Massive Dwarf zoom galaxies with and without BHs and found no preferential shift in the size- M_* plane. The source of this size increase seen for r556 may thus be random despite attempts to minimize

⁴ We shift the log y-intercept reported in Carlsten et al. (2021) (a_c) to account for the unit conversion in log space. Additionally, we shift the relation by $M_* = 5 \times 10^6 M_\odot$. So $a = a_c - 3 + b \log_{10}(5 \times 10^6) = 0.347$, where $a_c = 0.667$.

Test	Resolution	Star Formation	Feedback	Feedback Energy Budget	Black Holes
1 (fiducial)	Mint	H ₂	Superbubble	10 ⁴⁹ erg/M _⊙	Yes
2	Mint	H ₂	Superbubble	10 ⁴⁹ erg/M _⊙	No
3	Mint	NIHAO	Superbubble	10 ⁴⁹ erg/M _⊙	No
4	Near Mint	H ₂	Superbubble	10 ⁴⁹ erg/M _⊙	No
5	Near Mint	NIHAO	Superbubble	10 ⁴⁹ erg/M _⊙	No
6	Near Mint	NIHAO	BW	10 ⁴⁹ erg/M _⊙	No
7	Near Mint	NIHAO	BW + Early feedback	10 ⁴⁹ erg/M _⊙ + 2 × 10 ⁵⁰ erg/M _⊙	No

Table 2. Compact galaxy numerical experiments varying subgrid physics. The table lists the resolution of each associated subgrid variation along with the star formation prescription and feedback model used, as well as the feedback energy budget. The details of the H₂-based star formation model are found in Christensen et al. (2012), while the NIHAO star formation parameters are described in Wang et al. (2015). Superbubble feedback is described in Keller et al. (2014), while the blastwave (BW) feedback and early stellar feedback models are described in Stinson et al. (2006) and Stinson et al. (2013), respectively. The BH prescription used in our fiducial model is described in Tremmel et al. (2015) and Tremmel et al. (2017). Each variation is labeled by a test number, given in the first column.

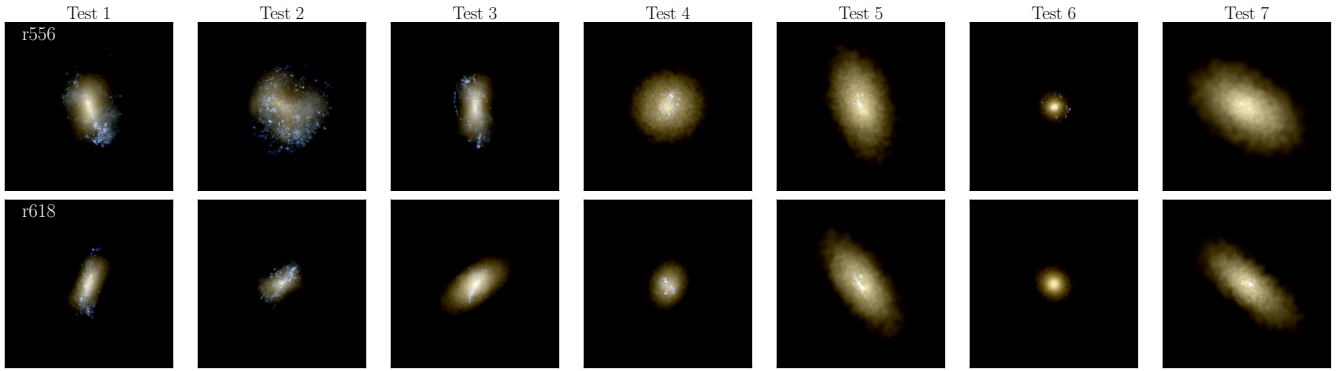


Figure 8. MOCK UVI IMAGES WITH DIFFERENT SUBGRID PHYSICS. Each panel has a side length of 15 kpc. The two different rows are for two simulations, r556 and r618, with the following physics in the columns, **first:** the fiducial H₂ star formation and superbubble feedback, **second:** H₂ star formation with superbubble feedback and no BHs, **third:** NIHAO star formation and superbubble feedback at the fiducial resolution, **fourth:** H₂ star formation, superbubble feedback at Near Mint resolution, **fifth:** NIHAO star formation and superbubble feedback at Near Mint resolution, **sixth:** NIHAO star formation with blastwave feedback, and **seventh:** NIHAO star formation with blastwave and early feedback. Test 7 is the closest to the original NIHAO simulation model. See text for details.

the impact of merger history. We conclude that there is no clear evidence that BHs are influencing the sizes or stellar masses of these dwarf galaxies.

6.2. Star Formation Model

The third column of Figure 8 (Test 3) builds upon Test 2 by altering the star formation model. As described in Section 2, our fiducial model follows the formation and destruction of H₂ and requires that H₂ be present when stars form. NIHAO uses density and temperature thresholds that allow stars to form at lower densities and higher temperatures than our fiducial model. However, changing the star formation model at this resolution does not preferentially alter the stellar half-light radius of each galaxy, as r556 becomes smaller (returning to roughly the size of the fiducial run) and r618 becomes larger (though only by $\sim 10\%$). In other

words, there is no clear evidence that changing the star formation prescription substantially impacts sizes at the fiducial Mint resolution.

However, we do find differences when going to lower resolution that we believe are influenced by the star formation model (discussed below). Hence, while we conclude that the star formation scheme yields similar-size galaxies at the fiducial resolution, we caution the reader that this might not be applicable under all circumstances.

6.3. Resolution

Since the mass resolution of the NIHAO galaxies in this halo mass range is lower than our fiducial resolution, we additionally explore tests at lower, Near-Mint resolution (see Section 2.3 for spatial and mass resolution details). The fourth column of Figure 8 shows

the results of Test 4, which is identical to Test 2 but at Near-Mint resolution, i.e., it is our fiducial model, minus BHs, but at lower resolution. Compared to the second column of the figure, the stellar sizes show no preferential change: r556 becomes $\sim 20\%$ larger, and r618 stays roughly the same.

Keeping the Near-Mint resolution the same, but changing to the NIHAO star formation model (Test 5) results in larger stellar sizes compared to Test 4. The same is true when comparing the results of Test 5 to those of Test 3 (which has the same physics, but at the higher Mint resolution). We conjecture that the change in size is due to the fact that a star formation model based on a density threshold is inherently resolution dependent. In the NIHAO star formation model, stars start to form right when the gas density crosses the star formation density threshold $n_* \geq 10.3 \text{ cm}^{-3}$ at both resolutions. As the resolution is lowered, the simulation loses the ability to resolve high-density peaks of gas. For reasons which are not understood, the lower resolution results in stars at larger radii (as can be seen in Figure 8). While the H_2 star formation model is not fully immune to resolution effects, the requirement that H_2 be present for star formation may act to keep sizes more stable because it limits star formation to regions with high densities, $n_* \geq 100 \text{ cm}^{-3}$. A full understanding of these effects requires additional work beyond the scope of this paper.

In summary, the NIHAO star formation model does lead to slightly larger galaxies at lower resolution, unlike our fiducial model. However, the change is not dramatic enough to explain the sizes of dwarfs seen in NIHAO.

6.4. Feedback

NIHAO also utilizes different feedback. The remaining two tests switch from superbubble feedback to blastwave. Test 6 is the same as Test 5, except for this one change. As is immediately obvious from the sixth column of Figure 8, the galaxies become much more compact after this switch. The reduction in size is in agreement with Mina et al. (2021), who found that dwarf galaxies simulated with blastwave feedback result in galaxies that have 2–3 \times smaller $r_{1/2}$ than the same systems run with superbubble. They conjecture that superbubble more strongly fluctuates the gravitational potential, which expands the radii of both dark matter (making cores) and stars, since both are collisionless particles (see, e.g., Graus et al. 2019; Riggs et al. 2024). However, sizes were *not* found to be different between the two feedback models in Azartash-Namin et al. (2024). While Mina et al. (2021) adopts a density threshold for star formation, Azartash-Namin et al.

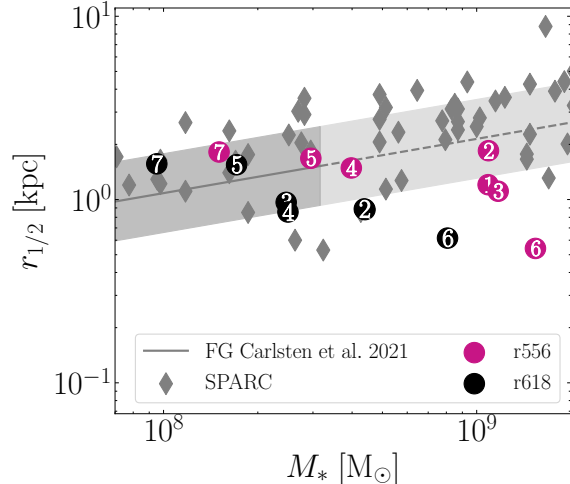


Figure 9. $r_{1/2}$ VERSUS M_* for galaxy r556 (magenta) and r618 (black), run with different subgrid physics. The marker number denotes the particular sub-grid physics test from Table 2. We note that Test 1 in r618 is sitting directly under Test 2. The SPARC data is shown by the gray diamonds, and the field size– M_* relationship is shown by the gray-shaded region for $M_* < 10^{8.5} M_\odot$ from Carlsten et al. (2021), with the extrapolation to higher masses indicated by the dashed line. The compact objects in Test 1 (fiducial model) progressively move from compact galaxies in the lower right of the size– M_* plane to the upper left; $r_{1/2}$ increases while stellar masses decrease.

(2024) adopts the same H_2 -based star formation as our fiducial model. This suggests again that the change in size may be dependent on the star formation model. However, it is clear that a change in feedback can yield dramatic size differences for a given galaxy.

Test 7 is the closest to the NIHAO simulations in Wang et al. (2015). Here, we add early stellar feedback to the physics of Test 6 as described in Section 2.3. The stellar sizes increase dramatically from Test 6, resulting in the largest galaxies across all the tests. As mentioned in Section 2.3, the early feedback model is tuned to limit star formation to agree with the abundance matching value at the Milky Way scale, neglecting the impacts on dwarf scales. This choice may be causing $r_{1/2}$ to be large below $M_* \sim 10^9 M_\odot$ (bottom panel of Figure 7). Beyond this, early feedback is added as thermal energy, similar to feedback from Type II SNe, though cooling is not shut off. This effectively gives a 20 \times boost (see feedback energy budgets in Table 2) to the total SN energy per star particle. Additionally, the energy is injected in a short time period, which likely helps maximize the effect. Given the change from Test 6 to Test 7, we conclude that the early feedback is the strongest contributor to making diffuse galaxies in NIHAO.

6.5. Summary: Changes in the Size–Mass Plane

Figure 9 presents the size– M_* relationship for galaxy r556 (magenta) and r618 (black) as each undergoes variations in its subgrid physics, following Table 2. Each test’s position in the size– M_* plane is plotted with its associated number. (Note that Test 1 in r618 is sitting directly under Test 2 in the figure.) The SPARC data is shown in gray diamonds, and we again present the observed size– M_* relationship with $1-\sigma$ in the shaded region from Carlsten et al. (2021), with the line styles as in Figure 7. The Mint resolution runs (Tests 1–3) cluster on the small side of the Carlsten et al. (2021) median relation, with some scatter. The Near Mint test with superbubble feedback and H_2 (Test 4) does not change much in size, though the stellar mass of r556 decreases, moving closer to the mean size– M_* relation. Switching to the NIHAO star formation scheme increases $r_{1/2}$ and further decreases stellar mass (Test 5), but switching to blastwave feedback (Test 6) makes the most compact galaxies, indicating that resolution alone is not limiting the production of compact galaxies. Including early feedback as in NIHAO makes the galaxies the most diffuse, while also decreasing their stellar mass (Test 7).

We have not reproduced the most diffuse NIHAO galaxies in the size– M_* plane, however, we have reproduced the most compact of the NIHAO galaxies (lower panel of Figure 7). Additionally, we have not achieved a perfect match to NIHAO with our Near Mint runs, only stepped in that direction (e.g., our particle masses and gas force resolution are slightly larger than theirs, our early feedback is a bit weaker, and we do not adopt a different, lower force resolution for the dark matter as they do). Test 6 makes it clear that resolution is not limiting the formation of compact galaxies. Further, given that the early feedback has the largest impact on size and stellar mass in our tests, we expect that increasing the early feedback efficiency from the value used here ($\epsilon_{\text{EF}} = 10\%$) to the value used in Wang et al. (2015) ($\epsilon_{\text{EF}} = 13\%$) would further increase sizes and decrease stellar masses. Still, the shift towards the upper left of the size– M_* plane is significant (M_* differs by 1-dex between Test 1 and Test 7 in r618), and the galaxies are nearly off the median relationship. The larger driver from the bottom right to the upper left of the size– M_* plane seems to be due partially to a resolution-dependent star formation model, in addition to very strong early stellar feedback. We conclude that the strong early feedback in NIHAO may prevent the formation of the most compact galaxies.

Until now, high-resolution simulations of galaxy formation have not been able to reproduce the full diversity of RCs in dwarf galaxies, at least before turning the simulated galaxies into mock observations of RCs (Roper et al. 2023). Our simulations are able to create dwarf galaxies that both rise more quickly and more slowly than predicted by an NFW profile, as measured by the midplane gravitational potential (bottom panels of Figure 3). The next subsections will discuss reasons why we might miss the most extreme objects. However, it is clear that the simulations presented here span a broader range of RC diversity than previously seen.

There has been a debate about whether feedback from baryons can solve the RC diversity problem. For example, Williams et al. (2025) predict dark matter density profiles within CDM using a theoretical model based on statistical mechanics. Their model shows that maximum entropy solutions for cold collisionless self-gravitating dark matter halos can have a range of inner density profiles, including flat density cores. They conclude that CDM density profiles can reproduce the whole range of diversity, without considering the contribution from baryons. On the other hand, Del Popolo et al. (2024) also used a large set of analytical, spherical collapse models to predict dark matter density profiles. Their models include the impact of baryonic feedback on dark matter density profiles. They conclude that the RCs follow the baryonic distribution, though we note that they still struggled to produce objects with the most quickly rising RCs in the $V_{\text{max}} \sim 70\text{--}100$ km/s range.

In galaxy simulations, the consensus to this point has been that baryons are responsible for creating the most slowly rising RCs in CDM, via the creation of dark matter cores from baryonic feedback (Santos-Santos et al. 2018, 2020). However, to date, no one has been able to simultaneously create dark matter cores and the most steeply rising RCs. These troubles have led to questions about whether baryonic feedback within CDM can produce the full range of diversity (Kaplinghat et al. 2020).

We conclude that the ability to simultaneously make quickly rising RCs is related to how dense the gas is allowed to get in the centers of the simulated galaxies. To form dwarfs with high surface densities, gas must be allowed to cool and form stars at the centers of halos, without being removed by strong feedback. The ability of the Marvel and Massive Dwarf simulations to simultaneously collect cold gas at their centers while also resolving clustered, bursty star formation allows them to be the first cosmological dwarf simulations to capture a broader range of RC diversity in the absence of mock RCs. In particular, these are the first simulations that

7. DISCUSSION

create dark matter cores while still allowing for steep RCs in compact galaxies.

7.1. Observational Considerations

While the simulations in this work produce a broader range of RC shapes than previous simulations, we still find a subset of SPARC galaxies in Figures 3, 4, and 5 that are more slowly rising than produced in the simulations. This subsection speculates how the inclusion of observational effects might impact these specific cases.

Many previous works have examined the origin of non-circular gas motions and their impact on observed RCs (e.g., Valenzuela et al. 2007). The feedback produced by bursty star formation histories in dwarf galaxies can drive them out of dynamical equilibrium (e.g., Read et al. 2016a; El-Badry et al. 2017; Verbeke et al. 2017; Downing & Oman 2023; Sands et al. 2024). Clustered SNe can create HI holes (Read et al. 2016b) inside galaxies, which can be hard to detect depending on the inclination angle (see also Verbeke et al. 2017; Sands et al. 2024), and feedback also drives non-circular motions such as turbulence or outflows. On top of feedback-induced non-circular motions, Marasco et al. (2018) showed that triaxial halos can induce radial gas flows (bars) in dwarf galaxies (see also Oman et al. 2019). Analytically derived RC speeds in triaxial halos deviate from spherical halos (see Binney & Tremaine 2008; Bovy in press 2026). Gas can also experience pressure support that reduces the velocity relative to stars and dark matter (Dalcanton & Stilp 2010; Oman et al. 2019; Pineda et al. 2017; Sands et al. 2024). Finally, because the relative contribution of rotational velocity is expected to decrease with decreasing galaxy mass, galaxies instead become dominated by dispersion and their disk thickness increases (Oman et al. 2019; Mancera Piña et al. 2022). This effect is likely to matter only in the lowest-mass galaxies, rather than our most-massive dwarfs, where diversity is maximized. However, the presence of dispersion, at all galaxy masses, is another factor that would lower observed rotation velocities (e.g., Jahn et al. 2023).

Many of the non-circular motions mentioned above tend to lower the velocities, particularly V_{fid} , relative to what we have presented here (Oman et al. 2019; Downing & Oman 2023). V_{fid} will be lowered because many of the processes discussed above are more centrally located, e.g., star formation rates are higher at the centers of galaxies, leading to more clustered star formation, feedback, and turbulence at the centers of galaxies. V_{max} can be lowered as well, but the result would be to shift r_{fid} to smaller radii and thus lower V_{fid} again.

If V_{fid} were to be lowered in mock observations, we can conjecture how our results would change (assuming that

V_{max} is largely unaffected). First, we would observe a broader range of V_{fid} in Figure 3 to lower velocities. The most slowly rising RCs are most likely to *appear* slowly rising due to non-circular motions (Oman et al. 2019; Roper et al. 2023). Second, lowering V_{fid} while keeping V_{max} unchanged will lower η_{rot} . While Σ_{bar} is not impacted (since the half-mass radius does not change), lowering η_{rot} might help to fill the space across all Σ_{bar} in the right panel of Figure 4. Finally, Roper et al. (2023) have already shown that lower V_{fid} shifts galaxies to lower η_{rot} and higher η_{bar} , i.e., galaxies shift into the lower-right corner in Figure 5.

While the most likely outcome of non-circular motion is a lowering of V_{fid} , Roper et al. (2023) also showed some instances where η_{rot} could increase. In particular, bisymmetrical non-circular motions (i.e., bars), such as those introduced within a triaxial halo, lead to sinusoidal variations in η_{rot} as azimuthal viewing angle changes (see their Figure 8). In some viewing angles, η_{rot} is much larger than the intrinsic value. We reproduce several galaxies with the steepest η_{rot} , but they tend to have lower V_{max} values than the SPARC data points with such high η_{rot} . While this might be simply small number statistics, it could be that such radial motions might bring some of our galaxies as high as the SPARC sample. The simulated galaxies predominantly reside in triaxial halos below $M_{\star} < 10^8 M_{\odot}$ (Keith et al. 2025), and we have witnessed the existence of bars in some of them (to be explored further in future work). Such radial motions might cause the most extreme steeply rising RCs.

7.2. The Role of Resolution

In this subsection, we explore how the ratios of dark matter to baryon particle mass impact RCs and stellar sizes. Numerical work has been conducted to examine where artificial two-body relaxation impacts central dark matter density profiles (Power et al. 2003; Ludlow et al. 2019a). Cosmological simulations often include mixtures of heavier dark matter and lighter baryonic particles. The unequal masses can result in so-called “mass segregation”⁵ as the particles try to reach energy equipartition, causing the more-massive particles to lose energy and fall inwards while the lower-mass particles heat up (Ludlow et al. 2019b).

In simulations where the stellar particles are less massive than their dark matter counterparts, stellar sizes can be artificially extended for low-mass systems at $z = 0$ (Ludlow et al. 2019b). The simulations presented in this work have large mass ratios between dark matter

⁵ This nomenclature is taken from Ludlow et al. (2019b).

and stars: $\mu = m_*/m_{\text{DM}} \sim 18$ for the Massive Dwarf zoom ins and $\mu \sim 15.8$ for the Marvel galaxies. This is because stars form with 30% the mass of their parent gas particles. Ludlow et al. (2019b) found that the convergence radius r_{conv} for two-body scattering, rather than the gravitational softening, sets the smallest stellar sizes obtainable. They additionally found that convergence was attained at all z when the stellar sizes exceeded r_{conv} . All the galaxy sizes in our simulation suites are larger than r_{conv} , as calculated in Section 4.2, which indicates that the stellar sizes should be converged.⁶

RCs are also influenced by large mass ratios between dark matter and star particles because of mass segregation. Ludlow et al. (2019b) found that dark matter RCs were only marginally impacted for large mass ratios ($\mu > 1$). However, the RCs associated with the stellar components were more significantly affected, with the full RC increasing in velocity with time more than the $\mu = 1$ case (see Figure 1 of Ludlow et al. 2019b).

Dark matter dominates the majority of our RCs at all radii. Larger μ values have little impact on the dark matter contribution to the RC. On the other hand, the most rapidly rising RCs in our sample are dominated by stars (see density profiles in Appendix C), and the baryonic component of RCs is strongly impacted by mass segregation. In the absence of mass segregation, RCs would rise even more quickly, particularly in the systems dominated by stars in the central regions. Hence, while mass segregation could be lowering V_{fid} in these galaxies, it does not negate the conclusion that we can make steeply rising RCs and hence that we make a broader range of RC diversity than previous hydrodynamical simulations within CDM.

8. SUMMARY AND CONCLUSIONS

This paper explored the diversity of dwarf galaxy properties in 85 simulated galaxies from the Massive Dwarf zoom ins and the Marvel Dwarf zoom volumes. We compared the properties of their simulated RCs and sizes to SPARC data (Lelli et al. 2016a). We found RCs that span a broader range of diversity than previously seen in Λ CDM simulations with baryons.

We explored the shapes of RCs, considering both the true halo V_{max} and that inferred when HI is resolved out to $1 M_{\odot} \text{ pc}^{-2}$. For the Massive Dwarfs, we find RCs that both rise slower and faster than the NFW prediction for $V_{\text{max}} \gtrsim 60 \text{ km/s}$ when RCs are calculated

using the gravitational midplane potential instead of the mass enclosed.

We also found for the first time that the simulated galaxies are a better match to the stellar size- M_* relationship, in contrast with previous simulations, which showed an offset in the size- M_* plane by $\gtrsim 1-2 \text{ kpc}$, with simulated galaxies more diffuse than observed (Jiang et al. 2019). Instead, we found dwarf galaxies from the Massive Dwarf zoom ins with diverse sizes at a fixed stellar mass, covering a similar area in the size- M_* plane as the SPARC galaxies and having similar power-law slopes, scatters, and offsets to the Carlsten et al. (2021) size- M_* power-law relationship.

We examined whether RC shapes are correlated with baryonic distributions, as previous works have drawn differing conclusions on this topic. We found the correlation varies with V_{max} . In a fixed bin of higher V_{max} , the most quickly rising RCs belong to more compact, high baryonic surface density galaxies, and the most slowly rising occurred in lower baryonic surface density galaxies. This is in agreement with previous work by Ren et al. (2019). However, this was not true for lower V_{max} systems, which showed a larger spread in RC shapes (measured by η_{rot}) at a fixed baryonic surface density, in line with Santos-Santos et al. (2020). We found significant diversity at lower surface densities and low baryon mass fractions within r_{fid} .

By re-running two of our most compact galaxies, we conclude that the early stellar feedback used in the NIHAO simulations likely prevents the formation of the most dense galaxies, leading to galaxies that are more diffuse than those observed (Jiang et al. 2019). Santos-Santos et al. (2020) showed that their EAGLE-CHT10 model, which has clustered, bursty star formation that leads to dark matter cores, also makes diffuse dwarf galaxies and none that are more quickly rising than NFW below $V_{\text{max}} \sim 100 \text{ km s}^{-1}$ (see also Roper et al. 2023). Although we were unable to rerun their models, it seems clear that they likely also have feedback strong enough to prevent the formation of compact galaxies.

However, there is a subset of the most slowly rising SPARC RCs with large baryon mass fractions that we were unable to reproduce, and this is apparent in multiple galaxy property planes. The existence of these slowly rising RCs with large baryon mass fractions and high surface densities remains physically perplexing. Simulations with stronger feedback do a better job of populating this region, but at the expense of making steeply rising RCs (Santos-Santos et al. 2020) and the most compact observed dwarf galaxies. We postulate that the RCs of these systems may be impacted by non-circular motions, as found using mock HI RCs in Roper et al.

⁶ Azartash-Namin et al. (2024) showed that stellar sizes in Marvel galaxies stop changing at $r_{1/2} \sim 0.34 \text{ kpc}$, smaller than the galaxies we consider here, but consistent with Ludlow et al. (2019b).

(2023). We also note that works that generate mock RCs should ensure and report that they are also able to properly produce the size– M_* relationship in dwarf galaxies to fully address the diversity of dwarfs problem. We do not perform a similar analysis in this paper, but hope to in future work.

We conclude that the ability to simultaneously make quickly rising RCs is related to how dense the gas is allowed to get in the centers of the simulated galaxies. To form dwarfs with high surface densities, gas must be allowed to cool and form stars at the centers of halos, without being removed by strong feedback. The ability of these ChaNGa dwarfs to simultaneously collect cold gas at their centers while also resolving clustered, bursty star formation allows them to be the first cosmological dwarf simulations in CDM to capture a broader range of size and RC diversity. In particular, these are the first CDM simulations that create dark matter cores while still allowing for steep RCs in compact galaxies.

It has also been argued that the diversity of RC shapes is better reproduced in a self-interacting dark matter (SIDM) model (Spergel & Steinhardt 2000) than in CDM (Kaplinghat et al. 2014; Ren et al. 2019; Kaplinghat et al. 2020). Assuming a low SIDM cross section allows dwarfs in this mass range to produce thermalized dark matter density cores that react to the potential of the baryonic distribution. In this model, RC shapes correlate with high and low surface brightness galaxies. However, the absence of the most compact objects in previous simulations will make producing diversity impossible for galaxies simulated in this SIDM case, as well as the CDM case. We will explore this in a forthcoming work.

9. ACKNOWLEDGEMENTS

APPENDIX

A. COMPARISON OF ROTATION CURVE SHAPE MEASUREMENT METHODS

The main text presents four different ways of measuring maximum and central velocities, V_{\max} and V_{fid} . Here, we present a direct comparison between methods for each of the Massive Dwarf zoom galaxies. We first compare the midplane method for deriving rotation curves (RCs) to the spherical mass-enclosed method (Equation 4 versus 3). The left panel of Figure A1 compares the mid+HI in dark purple to the circ+HI method in light purple, with a black line connecting the same galaxy measured with the two different approaches. If the galaxy has a stellar disk, it is denoted with an X marker; if it does not have a disk, it is marked with a circle. We use the specific angular momentum j of the stars to define disks. After aligning the galaxy in the x-y plane using the angular momentum vector of the gas in the central 5 kpc, galaxies with a median stellar z-component $j_z/j > 0.5$ are defined as disks. We find that galaxies with disks have larger V_{\max} and lower V_{fid} values. This is in agreement with the analytic prediction that RCs derived for disks using gravitational potentials peak at larger velocity and galactocentric radius compared to the spherical mass-enclosed case. Thus, disk galaxies shift to the lower right of the $V_{\text{fid}} - V_{\max}$ plane, sometimes falling below the NFW prediction when the mid+HI method is used. Non-disks also shift, with lower V_{\max} systems shifting more in V_{fid}

AC thanks Julianne Dalcanton, Nico Garavito Camargo, Adrian Price-Whelan, and Isabel Santos-Santos for helpful discussions on this work. AMB acknowledges support from NSF grant AST-2306340 and from grant FI-CCA-Research-00011826 from the Simons Foundation. ML is supported by the Department of Energy (DOE) under Award Number DE-SC0007968 and the Simons Investigator in Physics Award. AHGP is supported by National Science Foundation Grant No. AST-2008110 and AST-2510899. FDM acknowledges support from NSF grant PHY2013909. This research was supported in part by grant NSF PHY-2309135 to the Kavli Institute for Theoretical Physics (KITP). This work was performed in part at Aspen Center for Physics, which is supported by National Science Foundation grant PHY-2210452. BWK acknowledges support provided by NASA through a grant from the Space Telescope Science Institute, through grant HST AR-17547. This work used Stampede2 at the Texas Advanced Computing Center (TACC) through allocation MCA94P018 from the Advanced Cyberinfrastructure Coordination Ecosystem: Services & Support (ACCESS) program, which is supported by U.S. National Science Foundation grants 2138259, 2138286, 2138307, 2137603, and 2138296. Resources supporting this work were provided by the NASA High-End Computing (HEC) Program through the NASA Advanced Supercomputing (NAS) Division at Ames Research Center. Some of the simulations were performed using resources made available by the Flatiron Institute. The Flatiron Institute is a division of the Simons Foundation.

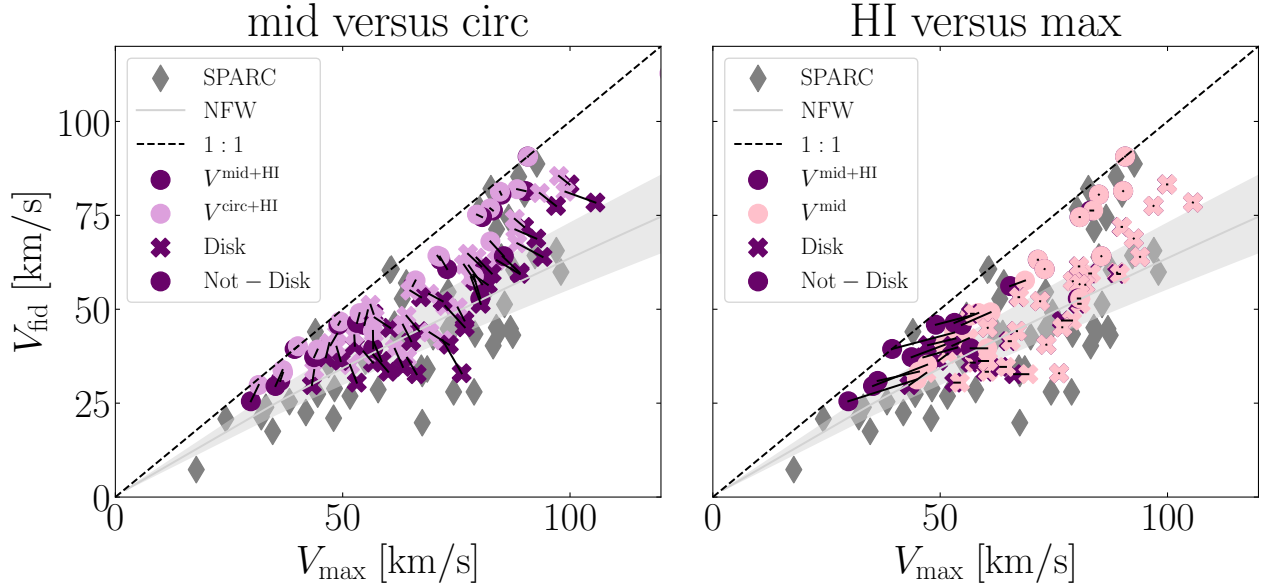


Figure A1. RC SHAPE MEASUREMENT COMPARISON for the Massive Dwarf galaxies. In both panels, the SPARC galaxies are shown in gray diamonds, the NFW prediction is the gray shaded region corresponding to the scatter in the mass-concentration relationship, and the black dashed line is the 1 : 1 line. Additionally, disk galaxies are denoted as X markers and the galaxies which are not disk are shown as circles. **Left:** A comparison between the mid+HI method (dark purple) and the circ+HI method (light purple) is shown. When disks are present the Massive Dwarfs shift to lower V_{fid} and larger V_{max} for the mid+HI compared to circ+HI. **Right:** A comparison between the mid+HI (dark purple) and the mid method (pink) is shown. For the higher-mass systems, there is little change between the two methods, and it is only at the low V_{max} end where galaxies start to have lower V_{max} and V_{fid} for the mid+HI compared to circ+HI case. This is because in the HI case, the RC is still rising at R_1 , causing a shift to lower V_{max} . This shift causes r_{fid} to be measured at a lower radius along the same RC curve, decreasing V_{fid} .

than V_{max} . As we discuss in the main text, this is likely due to the fact that the feedback in lower-mass galaxies can easily throw them out of dynamical equilibrium.

The right panel of Figure A1 compares the case where RCs are measured out to the true V_{max} versus that of truncating the RCs at R_1 to mimic observational limits. Most velocity measurements are unaffected above $V_{\text{max}} \sim 60$ km/s. For the lower-mass systems, galaxies shift to the lower left of the $V_{\text{fid}} - V_{\text{max}}$ plane, closer to or at the 1 : 1 line when the mid+HI is used instead of the mid method. In the lower-mass systems, there is less HI and R_1 decreases (see Ruan et al. 2025). The smaller R_1 leads to a decrease in the measured V_{max} . Thus, r_{fid} decreases since it is proportional to V_{max} , and V_{fid} also decreases.

B. THE IMPACT OF SUPERBUBBLE VERSUS BLASTWAVE FEEDBACK

Azartash-Namin et al. (2024) explored differences in burstiness of star formation and impact on dark matter density profiles in superbubble compared to blastwave feedback for the Marvel volume Storm galaxies. They also explored additional galaxy scaling relations. We select the galaxies in both Storm zoom volumes that match our stellar mass cut, and we match each halo in the two different runs using dark matter particle IDs as detailed in Azartash-Namin et al. (2024). In Figure B1, we show the pairs with the matches connected with black lines. The superbubble runs are shown in maroon and the blastwave runs in black. The mid+HI method is used in both cases. There is a preference towards larger V_{max} for a given galaxy in the runs with superbubble feedback. Azartash-Namin et al. (2024) noted a systematic increase in M_{vir} in the superbubble runs compared to the blastwave runs, likely translating to the preference for larger V_{max} in the superbubble compared to blastwave runs. For the lower-mass systems, the RCs are pushed towards or above the NFW prediction shown by the gray line. In the most massive system however, only V_{max} increases.

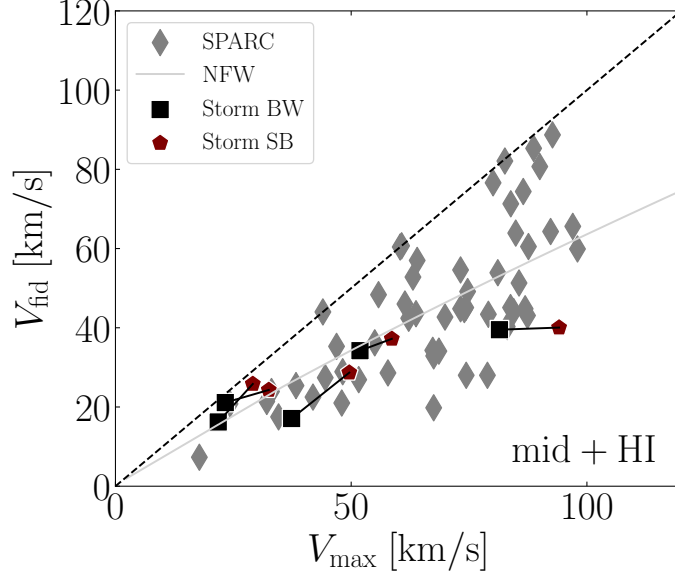


Figure B1. V_{fid} VERSUS V_{max} COMPARISON in galaxies run with superbubble (maroon pentagons) versus blastwave feedback (black squares), with SPARC data shown by the gray diamonds, and the NFW prediction is the gray. The black lines connect the same halo in the blastwave versus superbubble cases. There is a preference for higher V_{max} for galaxies with superbubble compared to those in blastwave.

C. DENSITY PROFILES

Figure C1 shows the density profiles (outside the convergence radius r_{conv}) for the 30 most-massive galaxies in the Massive Dwarf set. Using the simulation particle data, we show the spherically averaged densities for dark matter, gas, and stars in red, maroon, and orange, respectively. The sub-panels are ordered by M_* from top to bottom and left to right in a given row, with the simulation name in the upper right-hand corner of each sub-panel. The value of r_{fid} is indicated by the dashed black vertical line in each sub-panel.

We fit all $z = 0$ dark matter density profiles to a core-Einasto profile (Lazar et al. 2020),

$$\log \left[\frac{\rho_{\text{cEin}}(r)}{\rho_s} \right] = -\frac{2}{\alpha_\epsilon} \left[\left(\frac{r + r_c}{r_s} \right)^{\alpha_\epsilon} - 1 \right], \quad (\text{C1})$$

where ρ_s is a normalization parameter, r_c is the core radius, r_s is the scale radius, and $\alpha_\epsilon = 0.16$. We restrict the density profile fits to the radial range of r_{conv} to R_{200} . The lower bound is intended to limit artificial two-body heating at low radii (Power et al. 2003; Ludlow et al. 2019a).

Following Lazar et al. (2020), we quantify the goodness of fit using the quality factor Q , defined as

$$Q^2 = \frac{1}{N} \sum_i^N [\log_{10} \rho_i - \log_{10} \rho_i^{\text{fit}}]^2, \quad (\text{C2})$$

where N is the number of radial bins, and ρ^{fit} is the fit defined using Equation C1 with the relevant parameters chosen to minimize Q . The best-fit core-Einasto curve is shown as the dashed black curve in each sub-panel of Figure C1.

The slope of the dark matter density profile is

$$\frac{d \log \rho_{\text{cEin}}(r)}{d \log r} = -2 \left(\frac{r}{r_s} \right)^{\alpha_\epsilon} \left(1 + \frac{r_c}{r} \right)^{\alpha_\epsilon - 1} \quad (\text{C3})$$

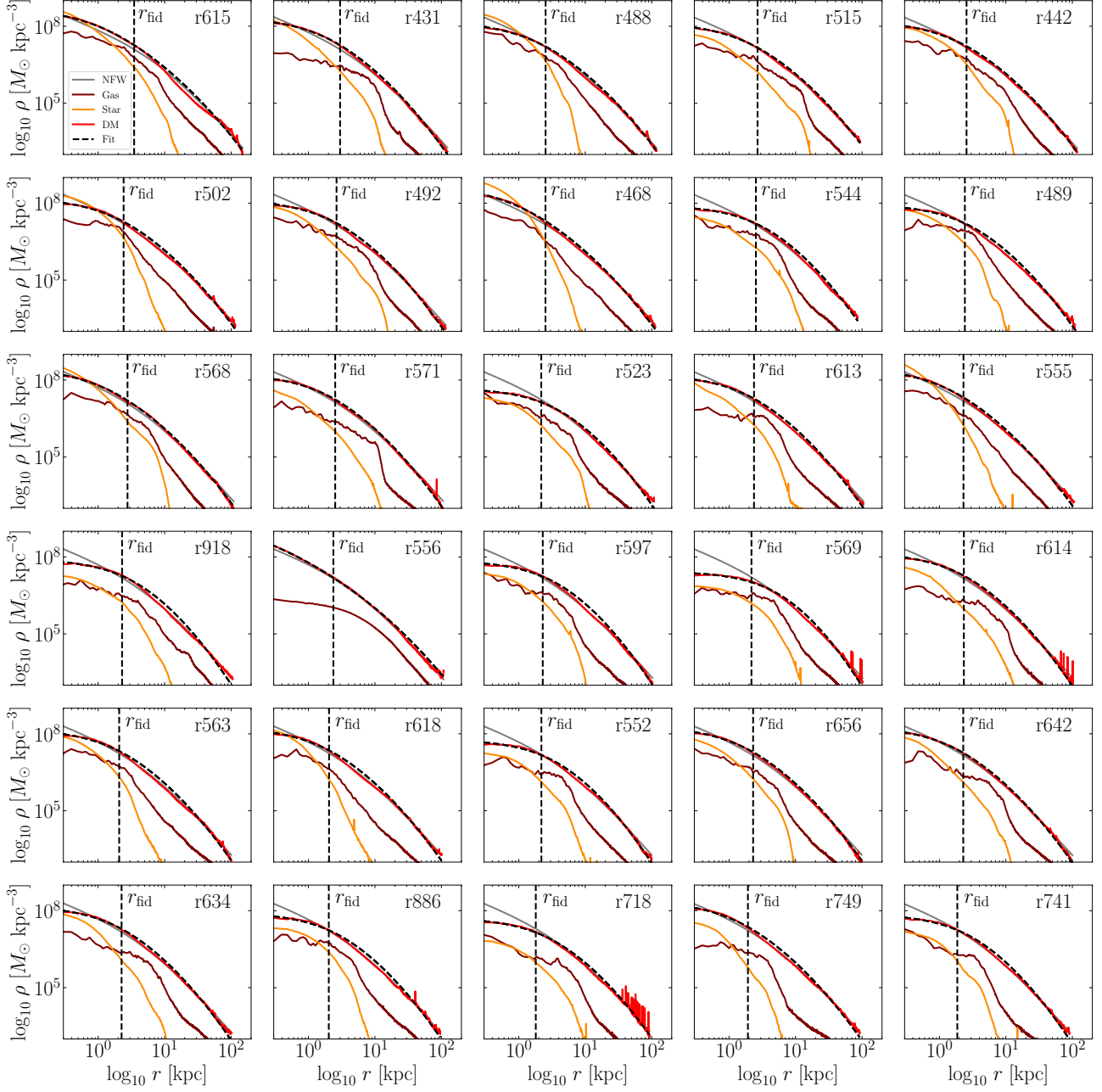


Figure C1. DENSITY PROFILES FOR THE 30 MOST-MASSIVE MASSIVE DWARF ZOOMS in maroon for gas, orange for stars, and red for dark matter. Cored Einasto fits are shown in black dashed lines and NFW in gray. The dashed black vertical line in each sub-panel indicates r_{fid} , the point where we measure the density slope α .

and is related to the inner slope of the RC, i.e., the shape of the inner RC. More explicitly, halos with central densities with slope α ($\rho \sim r^\alpha$) have central mass profiles

$$M(r) \sim \int_0^r dr' r'^{\alpha} r'^{-2} \sim r^{3+\alpha} \quad (\text{C4})$$

and the associated spherical mass-enclosed circular velocity profiles rise as

$$V_{\text{circ}} \sim \sqrt{r^{3+\alpha}/r} \sim r^{1+\alpha/2}. \quad (\text{C5})$$

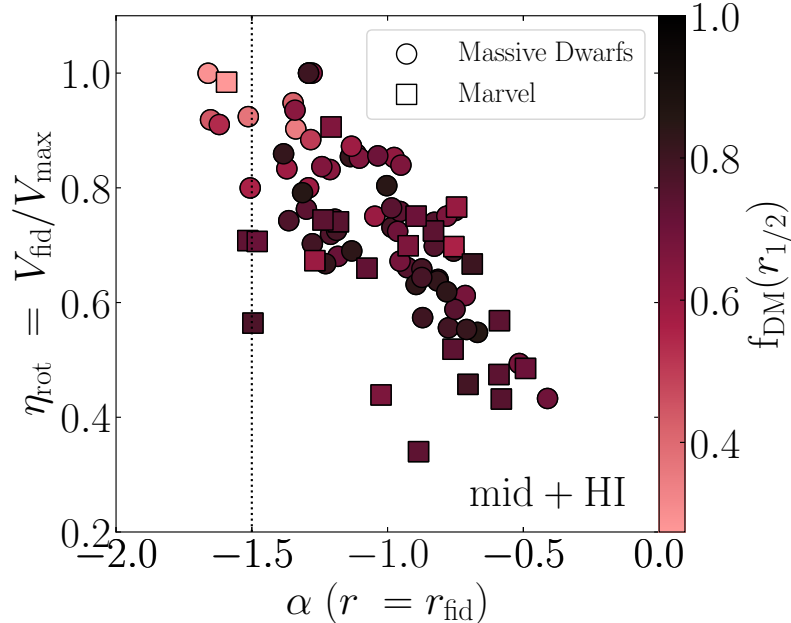


Figure C2. η_{rot} VERSUS INNER SLOPE α COLORED BY DARK MATTER MASS FRACTION WITHIN $r_{1/2}$, $f_{\text{DM}}(r_{1/2})$, for the Massive Dwarf (circles) and Marvel (squares) galaxies at $z = 0$. The inner slope α is measured at r_{fid} . More quickly (slowly) rising RCs have steeper (shallower) dark matter slopes.

When a disk is present, it will dominate the midplane potential, further altering the shape of the RCs (Binney & Tremaine 2008). As noted in Oman et al. (2015), the size of the core also influences the shape of RCs since V_{circ} depends on mass enclosed.

Figure C2 explores how the dark matter slope $\alpha(r_{\text{fid}})$ is related to the RC shape parameter η_{rot} , with points colored by the dark matter mass fraction within $r_{1/2}$. There is a clear correlation between η_{rot} and $\alpha(r_{\text{fid}})$. The most slowly rising objects have $\alpha(r_{\text{fid}}) \sim -0.5$ while the most quickly rising objects have $\alpha(r_{\text{fid}}) \lesssim -1.5$. The latter also have the smallest dark matter fractions; in these cases, prominent central stellar distributions dominate the total inner densities, setting the central velocities (Figure C1).

We also check the slopes in the corresponding dark-matter-only (DMO) Massive Dwarf zooms using the same fitting methods. These simulations have the same cosmology, gravitational softening, and dark matter particle-mass resolution as the hydro Massive Dwarf zooms. Measuring the slope at r_{fid} of the corresponding hydro run, we find $\alpha(r_{\text{fid}}) \sim -1.5$ in all cases. Thus, while the hydro simulations do not produce halos with central slopes $\alpha(r_{\text{fid}}) \sim 0$, most of the sample is still more cored than the corresponding DMO case. Moreover, r_{fid} is well outside of the dark matter core size. Only the most quickly rising systems have slopes slightly higher than DMO runs, likely because of the presence of a dense stellar component driving adiabatic contraction (Blumenthal et al. 1986; Dutton et al. 2005; Gnedin et al. 2011).

REFERENCES

- Arnett, D. 1996, *Supernovae and Nucleosynthesis: An Investigation of the History of Matter from the Big Bang to the Present*
- Azartash-Namin, B., Engelhardt, A., Munshi, F., et al. 2024, *ApJ*, 970, 40, doi: [10.3847/1538-4357/ad49a5](https://doi.org/10.3847/1538-4357/ad49a5)
- Bellovary, J. M., Cleary, C. E., Munshi, F., et al. 2019, *MNRAS*, 482, 2913, doi: [10.1093/mnras/sty2842](https://doi.org/10.1093/mnras/sty2842)
- Benavides, J. A., Sales, L. V., Wetzel, A., et al. 2025, arXiv e-prints, arXiv:2508.00991, doi: [10.48550/arXiv.2508.00991](https://doi.org/10.48550/arXiv.2508.00991)
- Benítez-Llambay, A., Frenk, C. S., Ludlow, A. D., & Navarro, J. F. 2019, *MNRAS*, 488, 2387, doi: [10.1093/mnras/stz1890](https://doi.org/10.1093/mnras/stz1890)
- Binney, J., & Tremaine, S. 2008, *Galactic Dynamics: Second Edition*

- Blumenthal, G. R., Faber, S. M., Flores, R., & Primack, J. R. 1986, *ApJ*, 301, 27, doi: [10.1086/163867](https://doi.org/10.1086/163867)
- Booth, C. M., & Schaye, J. 2009, *MNRAS*, 398, 53, doi: [10.1111/j.1365-2966.2009.15043.x](https://doi.org/10.1111/j.1365-2966.2009.15043.x)
- Bosma, A. 1981, *AJ*, 86, 1825, doi: [10.1086/113063](https://doi.org/10.1086/113063)
- Bovy, J. in press 2026, *Dynamics and Astrophysics of Galaxies* (Princeton, NJ: Princeton University Press)
- Bradford, J. D., Geha, M. C., & van den Bosch, F. C. 2016, *ApJ*, 832, 11, doi: [10.3847/0004-637X/832/1/11](https://doi.org/10.3847/0004-637X/832/1/11)
- Broeils, A. H., & Rhee, M. H. 1997, *A&A*, 324, 877
- Brook, C. B., Governato, F., Roškar, R., et al. 2011, *MNRAS*, 415, 1051, doi: [10.1111/j.1365-2966.2011.18545.x](https://doi.org/10.1111/j.1365-2966.2011.18545.x)
- Carlsten, S. G., Greene, J. E., Greco, J. P., Beaton, R. L., & Kado-Fong, E. 2021, *ApJ*, 922, 267, doi: [10.3847/1538-4357/ac2581](https://doi.org/10.3847/1538-4357/ac2581)
- Catinella, B., Giovanelli, R., & Haynes, M. P. 2006, *ApJ*, 640, 751, doi: [10.1086/500171](https://doi.org/10.1086/500171)
- Celiz, B. M., Navarro, J. F., Abadi, M. G., & Springel, V. 2025, *A&A*, 699, A12, doi: [10.1051/0004-6361/202554847](https://doi.org/10.1051/0004-6361/202554847)
- Christensen, C., Quinn, T., Governato, F., et al. 2012, *MNRAS*, 425, 3058, doi: [10.1111/j.1365-2966.2012.21628.x](https://doi.org/10.1111/j.1365-2966.2012.21628.x)
- Christensen, C. R., Brooks, A. M., Munshi, F., et al. 2024, *ApJ*, 961, 236, doi: [10.3847/1538-4357/ad0c5a](https://doi.org/10.3847/1538-4357/ad0c5a)
- Christensen, C. R., Governato, F., Quinn, T., et al. 2014, *MNRAS*, 440, 2843, doi: [10.1093/mnras/stu399](https://doi.org/10.1093/mnras/stu399)
- Collins, M. L. M., & Read, J. I. 2022, *Nature Astronomy*, 6, 647, doi: [10.1038/s41550-022-01657-4](https://doi.org/10.1038/s41550-022-01657-4)
- Crain, R. A., Schaye, J., Bower, R. G., et al. 2015, *MNRAS*, 450, 1937, doi: [10.1093/mnras/stv725](https://doi.org/10.1093/mnras/stv725)
- Dalcanton, J. J., & Stilp, A. M. 2010, *ApJ*, 721, 547, doi: [10.1088/0004-637X/721/1/547](https://doi.org/10.1088/0004-637X/721/1/547)
- de Blok, W. J. G. 2010, *Advances in Astronomy*, 2010, 789293, doi: [10.1155/2010/789293](https://doi.org/10.1155/2010/789293)
- de Blok, W. J. G., McGaugh, S. S., Bosma, A., & Rubin, V. C. 2001, *ApJL*, 552, L23, doi: [10.1086/320262](https://doi.org/10.1086/320262)
- Del Popolo, A., Le Delliou, M., & Lee, X. 2024, *arXiv e-prints*, arXiv:2410.05948, doi: [10.48550/arXiv.2410.05948](https://doi.org/10.48550/arXiv.2410.05948)
- Di Cintio, A., Brook, C. B., Dutton, A. A., et al. 2014a, *MNRAS*, 441, 2986, doi: [10.1093/mnras/stu729](https://doi.org/10.1093/mnras/stu729)
- Di Cintio, A., Brook, C. B., Macciò, A. V., et al. 2014b, *MNRAS*, 437, 415, doi: [10.1093/mnras/stt1891](https://doi.org/10.1093/mnras/stt1891)
- Downing, E. R., & Oman, K. A. 2023, *MNRAS*, 522, 3318, doi: [10.1093/mnras/stad868](https://doi.org/10.1093/mnras/stad868)
- Dutton, A. A., Buck, T., Macciò, A. V., et al. 2020, *MNRAS*, 499, 2648, doi: [10.1093/mnras/staa3028](https://doi.org/10.1093/mnras/staa3028)
- Dutton, A. A., Courteau, S., de Jong, R., & Carignan, C. 2005, *ApJ*, 619, 218, doi: [10.1086/426375](https://doi.org/10.1086/426375)
- Dutton, A. A., Macciò, A. V., Buck, T., et al. 2019, *MNRAS*, 486, 655, doi: [10.1093/mnras/stz889](https://doi.org/10.1093/mnras/stz889)
- El-Badry, K., Wetzel, A. R., Geha, M., et al. 2017, *ApJ*, 835, 193, doi: [10.3847/1538-4357/835/2/193](https://doi.org/10.3847/1538-4357/835/2/193)
- El-Badry, K., Quataert, E., Wetzel, A., et al. 2018, *MNRAS*, 473, 1930, doi: [10.1093/mnras/stx2482](https://doi.org/10.1093/mnras/stx2482)
- Flores, R. A., & Primack, J. R. 1994, *ApJL*, 427, L1, doi: [10.1086/187350](https://doi.org/10.1086/187350)
- Frank, B. S., de Blok, W. J. G., Walter, F., Leroy, A., & Carignan, C. 2016, *AJ*, 151, 94, doi: [10.3847/0004-6256/151/4/94](https://doi.org/10.3847/0004-6256/151/4/94)
- Frosst, M., Courteau, S., Arora, N., et al. 2022, *MNRAS*, 514, 3510, doi: [10.1093/mnras/stac1497](https://doi.org/10.1093/mnras/stac1497)
- Geda, R., Crawford, S. M., Hunt, L., et al. 2022, *AJ*, 163, 202, doi: [10.3847/1538-3881/ac5908](https://doi.org/10.3847/1538-3881/ac5908)
- Geda, R., Cruz, A., Wright, A. C., et al. 2025
- Genel, S., Bryan, G. L., Springel, V., et al. 2019, *ApJ*, 871, 21, doi: [10.3847/1538-4357/aaf4bb](https://doi.org/10.3847/1538-4357/aaf4bb)
- Gnedin, O. Y., Ceverino, D., Gnedin, N. Y., et al. 2011, *arXiv e-prints*, arXiv:1108.5736, doi: [10.48550/arXiv.1108.5736](https://doi.org/10.48550/arXiv.1108.5736)
- Governato, F., Brook, C., Mayer, L., et al. 2010, *Nature*, 463, 203, doi: [10.1038/nature08640](https://doi.org/10.1038/nature08640)
- Governato, F., Zolotov, A., Pontzen, A., et al. 2012, *MNRAS*, 422, 1231, doi: [10.1111/j.1365-2966.2012.20696.x](https://doi.org/10.1111/j.1365-2966.2012.20696.x)
- Graus, A. S., Bullock, J. S., Fitts, A., et al. 2019, *MNRAS*, 490, 1186, doi: [10.1093/mnras/stz2649](https://doi.org/10.1093/mnras/stz2649)
- Haardt, F., & Madau, P. 2012, *ApJ*, 746, 125, doi: [10.1088/0004-637X/746/2/125](https://doi.org/10.1088/0004-637X/746/2/125)
- Hopkins, P. F., Wetzel, A., Kereš, D., et al. 2018, *MNRAS*, 480, 800, doi: [10.1093/mnras/sty1690](https://doi.org/10.1093/mnras/sty1690)
- Jahn, E. D., Sales, L. V., Marinacci, F., et al. 2023, *MNRAS*, 520, 461, doi: [10.1093/mnras/stad109](https://doi.org/10.1093/mnras/stad109)
- Jiang, F., Dekel, A., Freundlich, J., et al. 2019, *MNRAS*, 487, 5272, doi: [10.1093/mnras/stz1499](https://doi.org/10.1093/mnras/stz1499)
- Kaplinghat, M., Keeley, R. E., Linden, T., & Yu, H.-B. 2014, *PhRvL*, 113, 021302, doi: [10.1103/PhysRevLett.113.021302](https://doi.org/10.1103/PhysRevLett.113.021302)
- Kaplinghat, M., Ren, T., & Yu, H.-B. 2020, *JCAP*, 2020, 027, doi: [10.1088/1475-7516/2020/06/027](https://doi.org/10.1088/1475-7516/2020/06/027)
- Keith, B., Munshi, F., Brooks, A. M., et al. 2025, *ApJ*, 986, 138, doi: [10.3847/1538-4357/add40d](https://doi.org/10.3847/1538-4357/add40d)
- Keller, B. W., Wadsley, J., Benincasa, S. M., & Couchman, H. M. P. 2014, *MNRAS*, 442, 3013, doi: [10.1093/mnras/stu1058](https://doi.org/10.1093/mnras/stu1058)
- Keller, B. W., Wadsley, J. W., Wang, L., & Kruijssen, J. M. D. 2019, *MNRAS*, 482, 2244, doi: [10.1093/mnras/sty2859](https://doi.org/10.1093/mnras/sty2859)

- Klein, C., Bullock, J. S., Moreno, J., et al. 2024, *MNRAS*, 532, 538, doi: [10.1093/mnras/stae1505](https://doi.org/10.1093/mnras/stae1505)
- Knollmann, S. R., & Knebe, A. 2009, *ApJS*, 182, 608, doi: [10.1088/0067-0049/182/2/608](https://doi.org/10.1088/0067-0049/182/2/608)
- Krause, M. G. H., Offner, S. S. R., Charbonnel, C., et al. 2020, *SSRv*, 216, 64, doi: [10.1007/s11214-020-00689-4](https://doi.org/10.1007/s11214-020-00689-4)
- Kroupa, P. 2001, *MNRAS*, 322, 231, doi: [10.1046/j.1365-8711.2001.04022.x](https://doi.org/10.1046/j.1365-8711.2001.04022.x)
- Kuzio de Naray, R., McGaugh, S. S., de Blok, W. J. G., & Bosma, A. 2006, *ApJS*, 165, 461, doi: [10.1086/505345](https://doi.org/10.1086/505345)
- Lazar, A., Bullock, J. S., Boylan-Kolchin, M., et al. 2020, *MNRAS*, 497, 2393, doi: [10.1093/mnras/staa2101](https://doi.org/10.1093/mnras/staa2101)
- Lelli, F., McGaugh, S. S., & Schombert, J. M. 2016a, *AJ*, 152, 157, doi: [10.3847/0004-6256/152/6/157](https://doi.org/10.3847/0004-6256/152/6/157)
- . 2016b, *ApJL*, 816, L14, doi: [10.3847/2041-8205/816/1/L14](https://doi.org/10.3847/2041-8205/816/1/L14)
- Lelli, F., Verheijen, M., Fraternali, F., & Sancisi, R. 2012, *A&A*, 544, A145, doi: [10.1051/0004-6361/201219457](https://doi.org/10.1051/0004-6361/201219457)
- Ludlow, A. D., Bose, S., Angulo, R. E., et al. 2016, *MNRAS*, 460, 1214, doi: [10.1093/mnras/stw1046](https://doi.org/10.1093/mnras/stw1046)
- Ludlow, A. D., Schaye, J., & Bower, R. 2019a, *MNRAS*, 488, 3663, doi: [10.1093/mnras/stz1821](https://doi.org/10.1093/mnras/stz1821)
- Ludlow, A. D., Schaye, J., Schaller, M., & Richings, J. 2019b, *MNRAS*, 488, L123, doi: [10.1093/mnrasl/slz110](https://doi.org/10.1093/mnrasl/slz110)
- Lupi, A., Volonteri, M., & Silk, J. 2017, *MNRAS*, 470, 1673, doi: [10.1093/mnras/stx1313](https://doi.org/10.1093/mnras/stx1313)
- Mancera Piña, P. E., Fraternali, F., Oosterloo, T., et al. 2022, *MNRAS*, 514, 3329, doi: [10.1093/mnras/stac1508](https://doi.org/10.1093/mnras/stac1508)
- Marasco, A., Oman, K. A., Navarro, J. F., Frenk, C. S., & Oosterloo, T. 2018, *MNRAS*, 476, 2168, doi: [10.1093/mnras/sty354](https://doi.org/10.1093/mnras/sty354)
- Marigo, P., Girardi, L., Bressan, A., et al. 2008, *A&A*, 482, 883, doi: [10.1051/0004-6361:20078467](https://doi.org/10.1051/0004-6361:20078467)
- Mashchenko, S., Wadsley, J., & Couchman, H. M. P. 2008, *Science*, 319, 174, doi: [10.1126/science.1148666](https://doi.org/10.1126/science.1148666)
- McGaugh, S. S., & Schombert, J. M. 2014, *AJ*, 148, 77, doi: [10.1088/0004-6256/148/5/77](https://doi.org/10.1088/0004-6256/148/5/77)
- McQuinn, K. B. W., Adams, E. A. K., Cannon, J. M., et al. 2022, *ApJ*, 940, 8, doi: [10.3847/1538-4357/ac9285](https://doi.org/10.3847/1538-4357/ac9285)
- Menon, H., Wesolowski, L., Zheng, G., et al. 2015, *Computational Astrophysics and Cosmology*, 2, 1, doi: [10.1186/s40668-015-0007-9](https://doi.org/10.1186/s40668-015-0007-9)
- Mina, M., Shen, S., Keller, B. W., et al. 2021, *A&A*, 655, A22, doi: [10.1051/0004-6361/202039420](https://doi.org/10.1051/0004-6361/202039420)
- Moore, B. 1994, *Nature*, 370, 629, doi: [10.1038/370629a0](https://doi.org/10.1038/370629a0)
- Munshi, F., Brooks, A. M., Applebaum, E., et al. 2021, *ApJ*, 923, 35, doi: [10.3847/1538-4357/ac0db6](https://doi.org/10.3847/1538-4357/ac0db6)
- Navarro, J. F., Frenk, C. S., & White, S. D. M. 1996, *ApJ*, 462, 563, doi: [10.1086/177173](https://doi.org/10.1086/177173)
- . 1997, *ApJ*, 490, 493, doi: [10.1086/304888](https://doi.org/10.1086/304888)
- Oh, S.-H., de Blok, W. J. G., Brinks, E., Walter, F., & Kennicutt, Robert C., J. 2011, *AJ*, 141, 193, doi: [10.1088/0004-6256/141/6/193](https://doi.org/10.1088/0004-6256/141/6/193)
- Oman, K. A., Marasco, A., Navarro, J. F., et al. 2019, *MNRAS*, 482, 821, doi: [10.1093/mnras/sty2687](https://doi.org/10.1093/mnras/sty2687)
- Oman, K. A., Navarro, J. F., Fattahi, A., et al. 2015, *MNRAS*, 452, 3650, doi: [10.1093/mnras/stv1504](https://doi.org/10.1093/mnras/stv1504)
- Petrosian, V. 1976, *ApJL*, 210, L53, doi: [10.1086/18230110.1086/182253](https://doi.org/10.1086/18230110.1086/182253)
- Pfalzner, S., Kaczmarek, T., & Olczak, C. 2012, *A&A*, 545, A122, doi: [10.1051/0004-6361/201219881](https://doi.org/10.1051/0004-6361/201219881)
- Piacitelli, D. R., Brooks, A. M., Christensen, C., et al. 2025, arXiv e-prints, arXiv:2505.08861, doi: [10.48550/arXiv.2505.08861](https://doi.org/10.48550/arXiv.2505.08861)
- Pineda, J. C. B., Hayward, C. C., Springel, V., & Mendes de Oliveira, C. 2017, *MNRAS*, 466, 63, doi: [10.1093/mnras/stw3004](https://doi.org/10.1093/mnras/stw3004)
- Planck Collaboration, Ade, P. A. R., Aghanim, N., et al. 2014, *A&A*, 571, A16, doi: [10.1051/0004-6361/201321591](https://doi.org/10.1051/0004-6361/201321591)
- Planck Collaboration, Aghanim, N., Akrami, Y., et al. 2020, *A&A*, 641, A6, doi: [10.1051/0004-6361/201833910](https://doi.org/10.1051/0004-6361/201833910)
- Pontzen, A., & Governato, F. 2012, *MNRAS*, 421, 3464, doi: [10.1111/j.1365-2966.2012.20571.x](https://doi.org/10.1111/j.1365-2966.2012.20571.x)
- Pontzen, A., Roškar, R., Stinson, G. S., et al. 2013, pynbody: Astrophysics Simulation Analysis for Python
- Pontzen, A., Governato, F., Pettini, M., et al. 2008, *MNRAS*, 390, 1349, doi: [10.1111/j.1365-2966.2008.13782.x](https://doi.org/10.1111/j.1365-2966.2008.13782.x)
- Power, C., Navarro, J. F., Jenkins, A., et al. 2003, *MNRAS*, 338, 14, doi: [10.1046/j.1365-8711.2003.05925.x](https://doi.org/10.1046/j.1365-8711.2003.05925.x)
- Read, J. I., Agertz, O., & Collins, M. L. M. 2016a, *MNRAS*, 459, 2573, doi: [10.1093/mnras/stw713](https://doi.org/10.1093/mnras/stw713)
- Read, J. I., & Gilmore, G. 2005, *MNRAS*, 356, 107, doi: [10.1111/j.1365-2966.2004.08424.x](https://doi.org/10.1111/j.1365-2966.2004.08424.x)
- Read, J. I., Iorio, G., Agertz, O., & Fraternali, F. 2016b, *MNRAS*, 462, 3628, doi: [10.1093/mnras/stw1876](https://doi.org/10.1093/mnras/stw1876)
- Regan, J. 2023, *The Open Journal of Astrophysics*, 6, 12, doi: [10.21105/astro.2210.04899](https://doi.org/10.21105/astro.2210.04899)
- Regan, J. A., Wise, J. H., Woods, T. E., et al. 2020, *The Open Journal of Astrophysics*, 3, 15, doi: [10.21105/astro.2008.08090](https://doi.org/10.21105/astro.2008.08090)
- Relatores, N. C., Newman, A. B., Simon, J. D., et al. 2019a, *ApJ*, 873, 5, doi: [10.3847/1538-4357/ab0382](https://doi.org/10.3847/1538-4357/ab0382)
- . 2019b, *ApJ*, 887, 94, doi: [10.3847/1538-4357/ab5305](https://doi.org/10.3847/1538-4357/ab5305)
- Ren, T., Kwa, A., Kaplinghat, M., & Yu, H.-B. 2019, *Physical Review X*, 9, 031020, doi: [10.1103/PhysRevX.9.031020](https://doi.org/10.1103/PhysRevX.9.031020)
- Riggs, C. L., Brooks, A. M., Munshi, F., et al. 2024, *ApJ*, 977, 20, doi: [10.3847/1538-4357/ad8b1e](https://doi.org/10.3847/1538-4357/ad8b1e)

- Roper, F. A., Oman, K. A., Frenk, C. S., et al. 2023, MNRAS, 521, 1316, doi: [10.1093/mnras/stad549](https://doi.org/10.1093/mnras/stad549)
- Ruan, D., Brooks, A. M., Cruz, A., et al. 2025, arXiv e-prints, arXiv:2503.16607, doi: [10.48550/arXiv.2503.16607](https://doi.org/10.48550/arXiv.2503.16607)
- Rubin, V. C., Ford, W. K., J., & Thonnard, N. 1980, ApJ, 238, 471, doi: [10.1086/158003](https://doi.org/10.1086/158003)
- Sales, L. V., Wetzel, A., & Fattahi, A. 2022, Nature Astronomy, 6, 897, doi: [10.1038/s41550-022-01689-w](https://doi.org/10.1038/s41550-022-01689-w)
- Sales, L. V., Navarro, J. F., Oman, K., et al. 2017, MNRAS, 464, 2419, doi: [10.1093/mnras/stw2461](https://doi.org/10.1093/mnras/stw2461)
- Sands, I. S., Hopkins, P. F., Shen, X., et al. 2024, arXiv e-prints, arXiv:2404.16247, doi: [10.48550/arXiv.2404.16247](https://doi.org/10.48550/arXiv.2404.16247)
- Santos-Santos, I. M., Di Cintio, A., Brook, C. B., et al. 2018, MNRAS, 473, 4392, doi: [10.1093/mnras/stx2660](https://doi.org/10.1093/mnras/stx2660)
- Santos-Santos, I. M. E., Navarro, J. F., Robertson, A., et al. 2020, MNRAS, 495, 58, doi: [10.1093/mnras/staa1072](https://doi.org/10.1093/mnras/staa1072)
- Schaye, J., Crain, R. A., Bower, R. G., et al. 2015, MNRAS, 446, 521, doi: [10.1093/mnras/stu2058](https://doi.org/10.1093/mnras/stu2058)
- Sérsic, J. L. 1963, Boletín de la Asociación Argentina de Astronomía La Plata Argentina, 6, 41
- Simon, J. D., Bolatto, A. D., Leroy, A., & Blitz, L. 2003, ApJ, 596, 957, doi: [10.1086/378200](https://doi.org/10.1086/378200)
- Spergel, D. N., & Steinhardt, P. J. 2000, PhRvL, 84, 3760, doi: [10.1103/PhysRevLett.84.3760](https://doi.org/10.1103/PhysRevLett.84.3760)
- Spergel, D. N., Bean, R., Doré, O., et al. 2007, ApJS, 170, 377, doi: [10.1086/513700](https://doi.org/10.1086/513700)
- Springel, V., Frenk, C. S., & White, S. D. M. 2006, Nature, 440, 1137, doi: [10.1038/nature04805](https://doi.org/10.1038/nature04805)
- Stinson, G., Seth, A., Katz, N., et al. 2006, MNRAS, 373, 1074, doi: [10.1111/j.1365-2966.2006.11097.x](https://doi.org/10.1111/j.1365-2966.2006.11097.x)
- Stinson, G. S., Brook, C., Macciò, A. V., et al. 2013, MNRAS, 428, 129, doi: [10.1093/mnras/sts028](https://doi.org/10.1093/mnras/sts028)
- Strauss, M. A., Weinberg, D. H., Lupton, R. H., et al. 2002, AJ, 124, 1810, doi: [10.1086/342343](https://doi.org/10.1086/342343)
- Teyssier, R., Pontzen, A., Dubois, Y., & Read, J. I. 2013, MNRAS, 429, 3068, doi: [10.1093/mnras/sts563](https://doi.org/10.1093/mnras/sts563)
- Tollet, E., Macciò, A. V., Dutton, A. A., et al. 2016, MNRAS, 456, 3542, doi: [10.1093/mnras/stv2856](https://doi.org/10.1093/mnras/stv2856)
- Tremmel, M., Governato, F., Volonteri, M., & Quinn, T. R. 2015, Monthly Notices of the Royal Astronomical Society, 451, 1868, doi: [10.1093/mnras/stv1060](https://doi.org/10.1093/mnras/stv1060)
- Tremmel, M., Governato, F., Volonteri, M., Quinn, T. R., & Pontzen, A. 2018, MNRAS, 475, 4967, doi: [10.1093/mnras/sty139](https://doi.org/10.1093/mnras/sty139)
- Tremmel, M., Karcher, M., Governato, F., et al. 2017, MNRAS, 470, 1121, doi: [10.1093/mnras/stx1160](https://doi.org/10.1093/mnras/stx1160)
- Valenzuela, O., Rhee, G., Klypin, A., et al. 2007, ApJ, 657, 773, doi: [10.1086/508674](https://doi.org/10.1086/508674)
- van der Wel, A., Straughn, A. N., Rix, H. W., et al. 2011, ApJ, 742, 111, doi: [10.1088/0004-637X/742/2/111](https://doi.org/10.1088/0004-637X/742/2/111)
- Verbeke, R., Papastergis, E., Ponomareva, A. A., Rath, S., & De Rijcke, S. 2017, A&A, 607, A13, doi: [10.1051/0004-6361/201730758](https://doi.org/10.1051/0004-6361/201730758)
- Wadsley, J. W., Keller, B. W., & Quinn, T. R. 2017, MNRAS, 471, 2357, doi: [10.1093/mnras/stx1643](https://doi.org/10.1093/mnras/stx1643)
- Wadsley, J. W., Stadel, J., & Quinn, T. 2004, NewA, 9, 137, doi: [10.1016/j.newast.2003.08.004](https://doi.org/10.1016/j.newast.2003.08.004)
- Wang, J., Koribalski, B. S., Serra, P., et al. 2016, MNRAS, 460, 2143, doi: [10.1093/mnras/stw1099](https://doi.org/10.1093/mnras/stw1099)
- Wang, L., Dutton, A. A., Stinson, G. S., et al. 2015, MNRAS, 454, 83, doi: [10.1093/mnras/stv1937](https://doi.org/10.1093/mnras/stv1937)
- Williams, L. L. R., Hjorth, J., & Skillman, E. D. 2025, arXiv e-prints, arXiv:2502.15879, doi: [10.48550/arXiv.2502.15879](https://doi.org/10.48550/arXiv.2502.15879)
- Wise, J. H., Regan, J. A., O'Shea, B. W., et al. 2019, Nature, 566, 85, doi: [10.1038/s41586-019-0873-4](https://doi.org/10.1038/s41586-019-0873-4)
- Zentner, A., Dandavate, S., Slone, O., & Lisanti, M. 2022, JCAP, 2022, 031, doi: [10.1088/1475-7516/2022/07/031](https://doi.org/10.1088/1475-7516/2022/07/031)